Doctoral theses at NTNU, 2020:278

Suraj Kumar Singh

Magneto-dynamic properties of thin films and interfaces

Doctoral thesis

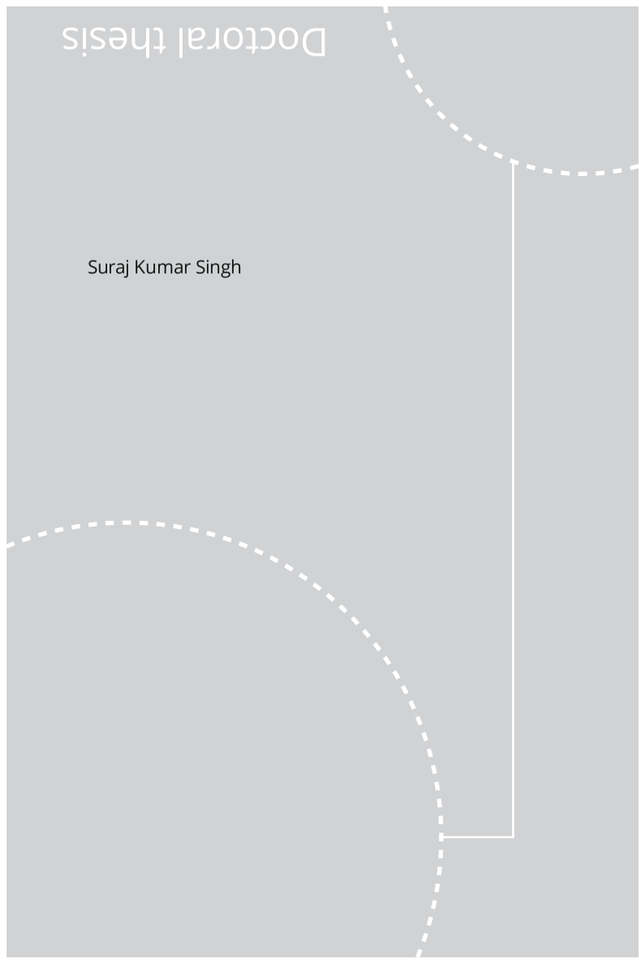

Suraj Kumar Singh

ISBN 978-82-326-4904-4 (printed ver.)
ISBN 978-82-326-4905-1 (electronic ver.)
ISSN 1503-8181

NTNU
Norwegian University of
Science and Technology

NTNU
Norwegian University of Science and Technology
Thesis for the Degree of
Philosophiae Doctor
Faculty of Natural Sciences
Department of Physics

Doctoral theses at NTNU, 2020:278

NTNU
Norwegian University of
Science and Technology

NTNU

Suraj Kumar Singh

Magneto-dynamic properties of thin films and interfaces

Thesis for the Degree of Philosophiae Doctor

Trondheim, September 2020

Norwegian University of Science and Technology
Faculty of Natural Sciences
Department of Physics

NTNU
Norwegian University of
Science and Technology

NTNU
Norwegian University of Science and Technology

Thesis for the Degree of Philosophiae Doctor

Faculty of Natural Sciences
Department of Physics

ISBN 978-82-326-4904-4 (printed ver.)
ISBN 978-82-326-4905-1 (electronic ver.)
ISSN 1503-8181

Doctoral theses at NTNU, 2020:278

Printed by NTNU Grafisk senter

To my parents

Abstract

Magnonics is a developing branch in the field of condensed matter physics with the potential to fulfill the future demand for miniaturized, fast, and energy-efficient spintronics devices. This thesis explores both a novel magnetodynamic system—the interface states in oxide system, as well as the tunability of dynamic properties due to nanostructuring in one-dimensional magnonic crystals (1D MCs). It also introduces a novel approach to propagating spin-wave spectroscopy that allows for higher sensitivity in characterization of low-damped materials.

The magnetodynamic properties of an induced magnetic state at complex oxide—$La_{0.7}Sr_{0.3}MnO_3$/$SrTiO_3$(LSMO/STO)(111)—heterostructure interface is investigated employing Ferromagnetic Resonance (FMR) spectroscopy. This study details the important characteristics of interface mode at LSMO/STO (111) interface. The study also discuss the complex structural or electronic and orbital reconstructions which could give rise to such interface magnetic state.

The investigation done on the magnetodynamic properties of dipole coupled 1D MCs explore the possibility to use dipolar coupling to tailor the static and magnetodynamic properties of MCs. The magnetodynamic properties have been investigated by two complementary FMR spectroscopies in combination with micromagnetic simulations and analytical calculations.The impact of dipolar coupling on the magnetodynamic damping is also presented.

An extension of the propagating spin-wave spectroscopy to a more sensitive field-sweep protocol is detailed. To this end the spin-wave propagation parameters investigated in Permalloy (NiFe) by two different excitation source—voltage pulse and continuous microwave have been investigated and compared. It is found that the continuous wave excitation allows for higher sensitivity measurements of a spin-wave mode in thinner films. This method has been used to investigate spin-wave propagation properties in half-metallic—Co_2FeAl Heusler alloy thin films.

Preface

This thesis is submitted to the Norwegian University of Science and Technology (NTNU) for partial fulfillment of the requirements for the degree Philosophiae Doctor (Ph.D.). It is based on 1 published and 3 unpublished work investigating the magnetodynamic properties of thin films and interfaces.

This work has been carried out at the Department of Physics at NTNU, under the supervision of Professor Erik Wahlstrom and co-supervision of Professor Thomas Tybell.

Trondheim, September 2020

Suraj Kumar Singh

Acknowledgements

It's my pleasure to acknowledge the role of many individuals who were instrumental in the completion of my Ph.D. thesis.

First of all, I would like to thank my supervisor Erik for his extraordinary support and guidance throughout my Ph.D. Without his help and insightful feedback this work would not be possible. I am extremely thankful for giving me the opportunity to work with him and for funding my research.

I am also very grateful to my co-supervisor Thomas who greatly assisted my research and was always willing to help me. His guidance, motivation, and consistent push in the right direction has been greatly appreciated.

I am grateful to all my coworkers who made my workplace less lonely. I would like to thank Vedran furtula for his assistance in laboratory work and for CST microwave simulations. I would like to express my sincere thanks to all the Nanolab engineers for providing excellent cleanroom facilities. I would like to thank Svenn Ove Linde for his assistance during my duty work in the cleanroom.

I would like to thank all my friends who made my stay in Trondheim enjoyable. Special thanks to Suneel, Surendra, Anjan, Piyush, and Indranil for playful cricket matches. I would also like to thank Shilpa and Anjan for their help during my initial stay in Trondheim.

I am extremely thankful to my parents for their love, prayers, caring, and sacrifices for my education and bright future. I am very thankful to my brother, sister, and my fiancée for their love and support.

List of papers

Paper I [1]:

Suraj Singh, Torstein Bolstad, Ingrid Hallsteinsen, Thomas Tybell, and Erik Wahlström.

Magnetodynamic properties of complex oxide—$La_{0.7}Sr_{0.3}TiO_3$/$SrTiO_3(111)$—heterostructure interface.

Applied Physics Letters **114** 222403, (2019).

Author contributions:

S.S.: Performed the FMR experiments. Performed data analysis and wrote the manuscript.
T.B. and I.H.: Provided samples and performed M-H measurements.
E.W. and T.T.: Supervised the project.

Paper II [2]:

Suraj Singh, Xiansi Wang, Ankit kumar, Alireza Qaiumzadeh, Peter Svendlindh, Thomas Tybell, and Erik Wahlström.

Mapping the dipolar coupling and magnetodynamic properties of dipole coupled 1D magnonic crystals.

Author contributions:

S.S.: Fabricated magnonic lattices, performed the cavity FMR measurements, analyzed data and wrote the manuscript.
X. W. and A. Q.: Performed analytical calculations and micromagnetic simulations.
A.K. and P. S.: Performed broadband FMR measurements.
E.W. and T.T.: Supervised the project.

Paper III [3]:

Suraj Singh, Vedran Furtula, Thomas Tybell, and Erik Wahlström.

Pulse versus continuous wave characterization of propagating spin waves in thin magnetic films.

Author contributions:

S.S.: Performed the propagating spin-wave spectroscopy measurements, analyzed data and wrote the manuscript.
V.F.: Assisted in developing propagating spin-wave spectroscopy.
E.W. and T.T.: Supervised the project.

Paper IV [4]:

Suraj Singh, Nanhe Kumar Gupta, Soumyarup Hait, Sujeet Chaudhary, Thomas Tybell, and Erik Wahlström.

Propagation properties of spin wave in Co_2FeAl, half-metallic Heusler alloy, ultrathin film.

Author contributions:

S.S.: Performed the propagating spin-wave measurements, analyzed data and wrote the manuscript.
N.K.G. and S.H.: Deposited Co_2FeAl thin films.
S.C.: Supervised the Co_2FeAl thin film growth.
E.W. and T.T.: Supervised the project.

List of main abbreviations

CAIBE	Chemically assisted ion beam etching
CMOS	Complementary metal oxide semiconductor
CMR	Colossal magnetoresistance
DMI	Dzyaloshinskii-Moriya interaction
FMR	Ferromagnetic resonance
GGG	Gadolinium gallium garnet
GMR	Giant magnetoresistance
IBE	Ion beam etching
LLG	Landau Lifshits Gilbert
LSMO	Lanthanum strontium manganate
MCs	Magnonic crystals
MRAM	Magnetic random-access memory
MSBVW	Magnetostatic backward volume wave
MSFVW	Magnetostatic forward volume wave
MSSW	Magnetostatic surface wave
PEC	Proximity effect correction
PSSW	Perpendicular standing spin-waves
PSWS	Propagating spin-wave spectroscopy
RIBE	Reactive ion beam etching
STO	Strontium titanate

STT	Spin transfer torque
TMJs	Magnetic tunnel junctions
TMR	Tunneling magnetoresistance
YIG	Yttrium iron garnet

Contents

Chapter 1

Introduction

Ever since the discovery of magnetism in naturally occurring mineral called *lodestone*, it has been an interesting topic of research for the science community. In the beginning called a magic stone, at present a most interesting branch of physics with a potential to change the whole world, the understanding of magnetism has evolved considerably. The development done in the last couple of hundreds of years in this research field has made an important impact on science as we know today. The incorporation of technologies developed based on the magnetic phenomenon has completely revolutionized our society and has huge scope in the future for potential miniaturized high-speed devices based on magnetism.

In conventional electronics where one uses the electron's charge degree of freedom as the carrier of information, the idea that electron's spin degree of freedom can also be used to serve the same purpose gives birth the field called spintronics [1]. The concept of electron spin was known for long, but its practical application in device came after the discovery of Giant magnetoresistance (GMR) in 1988, which awarded a Nobel prize to two physicists—Albert Fert and Peter Grunberg in 2007, in the form of GMR read head for hard disc drives [2–4]. The tunneling magnetoresistance (TMR) observed between two ferromagnets separated by an insulator is utilized in magnetic tunnel junctions (TMJs) [5–8]. At the same time the spin transfer torque (STT) phenomenon was discovered as tool to manipulate the magnetization orientation of magnetic layer by the charge current. The charge current become spin polarized after traversing through the ferromagnet and exert a torque on the magnetization with tendency to align the magnetization direction along the polarization direction of spin current [9, 10]. The magnetization manipulation by the spin current is main driving force for the realization of magnetic random-access memory (MRAM) [11, 12], spin transfer torque nano-

oscillators [13–15], magnetic domain-wall racetrack memory [16], and magnonic devices [17, 18].

Spin waves, a collective excitation of spins in the magnetic materials, have attracted significant attention of science community for their potential application in spintronic and magnonic devices [19, 20]. Magnons, the quanta of spin waves are building block of an emerging field called magnon spintronics or magnonics [21]. A concept that the spin waves can be used for information transport and data processing have motivated scientific community to investigate and develop proper understanding to control and manipulate spin waves for future technology applications.

Magnonics offers fast and energy-efficient spin-wave based computing technologies free from drawbacks inherent to modern electronics. However, there are fundamental and technological challenges. One of the main bottleneck is the materiel's Gilbert damping parameter. The spin-wave attenuates as it propagates in the material. The distance over which the spin-wave or information can travel is limited by the material's Gilbert damping parameter. Therefore, materials with low gilbert damping are crucial for the magnonic devices to be operational. Various metallic, half-metallic and insulating ferromagnets such as NiFe, CoFe, Co_2FeAl, YIG has been studied widely because of its low Gilbert damping and potential technological applications. For the fundamental and application point of view each material has their own advantages and disadvantages. For example, NiFe which is the top pick among the metallic ferromagnets, suffers from high damping because of magnon scattering by conduction electrons [22]. Consequently, attention moved towards the insulating ferromagnets. Yttrium iron garnet (YIG) is well known for its ultralow Gilbert damping ($\alpha \approx 10^{-5}$) which supports spin-wave propagation over millimeter distance [23, 24]. However, it has been widely deposited on Gadolinium Gallium Garnet (GGG) which is not compatible with CMOS technology. YIG, thus can be served as a model system whose technological application is limited [25]. Accordingly, it is important to study materials with low Gilbert damping as well as compitable with CMOS technology. Half-metallic ferromagnets in this regard are promising because of their interesting static and magneto-dynamic properties. The high degree of spin polarization selectively reduce some channels in the magnetization relaxation process [26] and thus reduces the magnetic damping. These interesting properties make the half-metallic ferromagnets a potential candidate for both spintronics and magnonics. Investigating magnetodynamic as well as understanding fundamental physics in such materials is thus crucial for their successful application in devices.

An active control and effective manipulation of spin waves is also a key issue for the magnonic devices to be operational. Magnonic crystals (MCs) which

are basically periodic modulated ferromagnets, offers a efficient way to control and manipulate the spin-wave properties. MCs have attracted considerable interest of scientist community for their potential applications in microwave filters [27], resonators [28], logic gates [29] and memory devices [30]. Particularly for memory applications, it has been demonstrated that each single element (lattice) of a densely packed 2D MCs can be used to save a bit and can boost the storage capacity [31]. However, this requires a very advance lithography techniques to make such small patterns. Thanks to electron beam lithography which makes it possible to fabricate MCs down to sub-nanometer scale. Increasing memory density by scaling down the bit size is however not straight forward because at nanoscale inter-lattice dipolar coupling dominates which make the physics much more complicated and challenging. Thus, the fundamental understanding the dipolar coupling is crucial both for underlying physics as well as for practical applications. Our study done on the magnetodynamic properties of dipole coupled 1D MCs focuses on dipolar coupling. The effect of inter-lattice spacing and lattice width on dipolar coupling have been investigated.

Outline of the thesis

This thesis is organized as follows: In chapter 2, the theoretical background which forms the basis of the thesis is presented. This chapter describes the various possible magnetic interactions, the basics of magnetization dynamics, magnetization relaxations, current-induced spin transfer torque, and micromagnetic simulations. Chapter 3 gives a brief introduction and state of art of the model material systems used in this thesis. In chapter 4, all the experimental tools used in sample fabrication as well as the techniques utilized in sample characterizations are introduced. Chapter 5 is devoted to a home built experimental setup propagating spin-wave spectroscopy (PSWS) to study the propagation characteristics of spin-wave in ferromagnetic thin films. This chapter covers the operating principle of PSWS, the fabrication process for the spin-wave device, the experimental design of setup and signal processing. At last, the paper and manuscripts which were published/written during my Ph.D. work are appended.

Chapter 2

Fundamentals of magnetization dynamics

This chapter describes the fundamentals of magnetization dynamics in ferromagnets. It will provide a theoretical background for the work performed in this thesis. Prior to discussing magnetization dynamics, the basics of magnetism and various possible magnetic interactions will be introduced. The Landau Lifshits Gilbert (LLG) equation describing magnetization dynamics will be introduced to understand the ferromagnetic resonance and spin-waves in ferromagnets. An overview of magnetization relaxation processes and current-induced spin-transfer torque will be discussed at the end of this chapter.

2.1 Magnetism in solids

The magnetic moment of an electron caused by its intrinsic properties of spin and charge is the origin of magnetism in solids. A strong interaction present in ferromagnetic material aligns the spins in a particular crystallographic direction which results in net magnetic moments in the material. The net magnetic moment per unit volume is called magnetization. In the preceding sections, the dynamic of the magnetization will be discussed.

The magnetic interaction energies in the confined structures of the ferromagnets play an important role and govern the magnetization dynamics at the nanoscale. A brief introduction of various magnetic interactions will be given prior to discussing the magnetization dynamics.

2.2 Energy Formulation

The magnetic ground state in ferromagnets results from the interplay of various magnetic interaction energies present in the system. The magnetic ground state can be obtained by minimizing the total magnetic energy present in the ferromagnet. The sum of relevant energies is given by the following equation:

$$\epsilon_{tot} = \epsilon_{zee} + \epsilon_{dem} + \epsilon_k + \epsilon_{ex} \tag{2.1}$$

where, ϵ_{zee} is the Zeeman energy, ϵ_{dem} the demagnetization energy, ϵ_k the anisotropy energy, and ϵ_{ex} the exchange energy. The effective magnetic field inside the magnet is given by:

$$H_{eff} = -\frac{\partial \epsilon_{tot}}{\partial M} \tag{2.2}$$

2.2.1 Zeeman Energy

The Zeeman energy is the interaction energy between the magnetization M, and the applied magnetic field H_{ext} and given by the expression:

$$\epsilon_{zee} = -\mu_0 \oint_V H_{ext} \cdot M dV \tag{2.3}$$

The energy is minimized when the magnetization get aligned along the applied field direction. Thus, the Zeeman energy makes it possible to manipulate the magnetic ground state by the applied magnetic field.

2.2.2 Demagnetization Energy

The demagnetization field is the magnetic dipolar field generated by the magnetization in the ferromagnet. It is also called stray field or dipolar field. Its origin can be explained by the Maxwell's equation. From the Gauss'law of magnetic flux conservation.

$$\nabla \cdot B = 0 \tag{2.4}$$

The magnetic flux density inside a ferromagnetic, $B = (H + M)$

$$\nabla \cdot B = \nabla \cdot (H + M) = 0 \tag{2.5}$$

$$\nabla \cdot H = -\nabla \cdot M \tag{2.6}$$

As we know the magnetization M of a magnetized body reduced to zero at the surface, and therefore at surface $\nabla \cdot M \# 0$. Hence, the field H which originates

from the term $\nabla \cdot M \# 0$ can be explained as field lines generated by magnetic poles on the surface of the magnet and is referred as demagnetization field. The energy associated with demagnetization field is called demagnetization energy:

$$\epsilon_{dem} = -\frac{\mu_0}{2} \oint_V H_D \cdot M dV \tag{2.7}$$

The demagnetization field depends on the sample geometry as well as on the magnetic state of the ferromagnets. Its complex dependence on position makes it hard to calculate the demagnetization field in an arbitrarily shaped ferromagnet. The demagnetization field is linearly related to magnetization by a geometry dependent constant called demagnetization tensor, $\tilde{N}$ in a uniformly magnetized ellipsoid and is given by the following relation [32]:

$$H_D = -\tilde{N} \cdot M \tag{2.8}$$

When the coordinate axes are chosen along the principle axes of the ellipsoid, the demagnetization tensor is given by a diagonal matrix:

$$\tilde{N} = \begin{pmatrix} N_x & 0 & 0 \\ 0 & N_y & 0 \\ 0 & 0 & N_z \end{pmatrix} \tag{2.9}$$

where, $N_{x,y,z}$ are demagnetization constant along x, y and z directions such that $N_x + N_y + N_z = 1$. The demagnetization tensor $\tilde{N}$ can be analytically calculated for the different sample geometries. For example, for thin films: $N_x = 0, N_y = 0, and N_z = 1$. For infinitely extended one-dimensional magnetic stripes with thickness $(t) \ll width(w)$: $N_x = 0, N_y = 2t/\pi w$, and $N_z = 1 - \frac{2t}{\pi w}$.

2.2.3 Anisotropy Energy

The crystalline ferromagnets are generally not isotropic. The magnetic properties vary in the direction in which they are measured. The magnetization prefers to align along a certain crystallographic direction called the easy axis of the ferromagnet. The energy associated with the rotation of the magnetization away from the easy axis is called magnetocrystalline energy. The magnetocrystalline energy originates from spin-orbit coupling and depends on the orientation of electron spins relative to crystallographic directions. In addition to magnetocrystalline anisotropy, there are other factors that also have a profound impact on the spin-orbit coupling. The epitaxial strain due to the lattice mismatch in thin films induces an anisotropy called stress anisotropy [33].

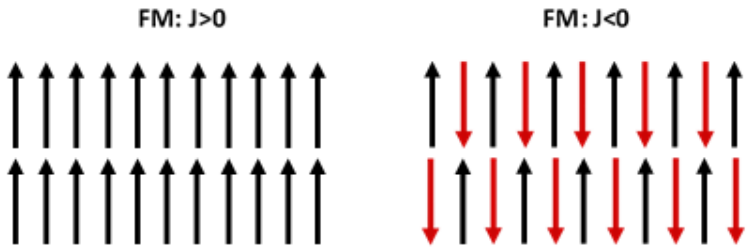

Figure 2.1: Schematic illustrating the ferromagnetic (left) and antiferromagnetic (right) ordering of spins for the positive and negative value of exchange interaction.

The simplest example of the anisotropy in ferromagnet is uniaxial magnetic anisotropy described by the expression:

$$\epsilon_k = -K_u sin^2\theta \tag{2.10}$$

where, K_u is the uniaxial anisotropy constant, and θ the angle between easy axis and magnetization vector.

2.2.4 Exchange Energy

Exchange interaction is the quantum mechanical effect responsible for spontaneous magnetization in ferromagnets. It originates from the combined effect of the Pauli exclusion principle and electrostatic Coulomb interaction. If we consider two adjacent electrons having spin angular momentum S_i and S_j, the total energy of the system according to the Heisenberg exchange model is given by [34]:

$$\epsilon_{ex} = -\frac{1}{2}\sum_{i<j} J_{ij} S_i \cdot S_j \tag{2.11}$$

where, J_{ij} is the exchange integral. The sign and strength of exchange integral determines the configuration of neighboring spins.

A positive value of the exchange interaction $J_{ij} > 0$ favors parallel alignment of the neighboring spins resulting in ferromagnetic (FM) order, whereas its negative value favors antiparallel alignment of spin resulting in antiferromagnetic ordering. Fig.2.1 illustrates the ferromagnetic and the antiferromagnetic ordering of the spins in a magnetic system.

On microscopic level where magnetization is regarded as continuous vector field, the expression for exchange energy through phenomenological continuum model

can be written as [35]:

$$\epsilon_{ex} = -\frac{A_{ex}}{M^2} \oint_V (\nabla \cdot M)^2 dV \tag{2.12}$$

where, A_{ex} represent the exchange stiffness.

2.3 Magnetization Dynamics

The aim of this section is to introduce the fundamentals of magnetization dynamics in the ferromagnets which form the basis of this thesis. The spins start precessing when perturbed by an external source. They precess with a particular phase and with a frequency in the gigahertz regime. Depending on the phase shift between neighboring spins, and on the propagation direction of resulting wave-like disturbance, many types of eigenmodes can be excited. To understand the various possible eigenmodes of such excitations, we will first start discussing the dynamics of a single electron spin in the static magnetic field. The collective behavior of all the spins together which is generally termed as magnetization dynamics in ferromagnets will be discussed.

2.3.1 Larmor precession

The energy of an electron having magnetic moment μ_S, in presence of a magnetic field is given by Zeeman energy:

$$E_S = -\mu_S \cdot H \tag{2.13}$$

This results in spin alignment along the direction of magnetic field according to energy minimization concept. The magnetic moment of the electron is related to its spin angular momentum, *S*:

$$\mu_S = -\gamma_S S \tag{2.14}$$

where, $\gamma_S = g_S \frac{e}{2m_e}$ is the gyromagnetic ratio. Here, e the electron charge, g_S the electron spin g-factor and m_e the electron mass. The toque acting on magnetic moment as a result of applied magnetic given by [34]:

$$\tau = \mu_S \times H \tag{2.15}$$

Since the rate change of the angular momentum is equal to torque (Newton's second law), the above two equations can be combined to:

$$\frac{d\mu_S}{dt} = -\gamma_S \mu_S \times H \tag{2.16}$$

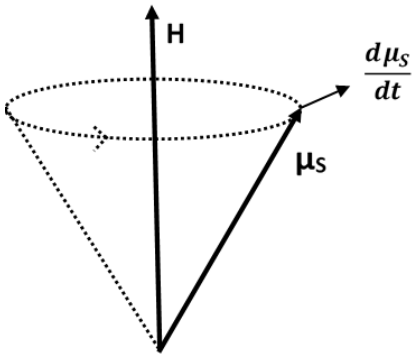

Figure 2.2: Schematic illustrating precession of electron's magnetic moment μ_S around the applied magnetic field (H)

This gives the equation of motion of electron's magnetic moment in presence of the magnetic field. It is obvious that the electron first starts precessing around the applied field before getting aligned along the field. Fig.2.2 illustrates the precession of electron's magnetic moment in presence of applied magnetic field. Solving the Eq.(2.16), one can find electron's precession frequency also called Larmor frequency given by:

$$\omega_L = \gamma_S H \tag{2.17}$$

2.3.2 The Landau-Lifshits-Gilbert equation

The equation of motion for the collection of spins in ferromagnet can be written with the help of Eq.(2.16), where the total moment is taken as a sum of individual electron magnetic moment in the classical approach [36].

$$\frac{dM}{dt} = -\gamma M \times H_{eff} \tag{2.18}$$

where, γ is the gyromagnetic ratio, M the magnetization of the ferromagnet. This equation describes the uniform precession of the magnetization around the effective field and known as Landau Lifshits (LL) equation. Since the spins precess in magnetic media, their motion are damped by dissipative forces present in the system as illustrated in Fig.2.3. To take the dissipative forces into account, Gilbert added a phenomenologic damping term in LL equation to describe the dynamics of spins in ferromagnets known as Landau Lifshits Gilbert (LLG) equation [37].

$$\frac{dM}{dt} = -\gamma M \times H_{eff} + \frac{\alpha}{M_S}\left[M \times \frac{dM}{dt}\right] \tag{2.19}$$

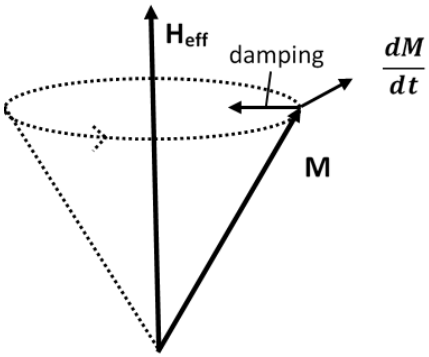

Figure 2.3: Schematic illustrating precession of magnetization (M) around the applied magnetic field (H). The magnetic damping acts against the precessional motion and relaxes the magnetization along the effective magnetic field.

where, α is a phenomenologic dimensionless damping parameter also known as Gilbert damping parameter. The Gilbert damping in an important parameter crucial for the realization of spin-based devices. Thus, understanding the various possible mechanisms responsible for the damping is important. These processes have been categorized into two groups - extrinsic and intrinsic. The details of the damping processes will be discussed later in the section.

2.3.3 Ferromagnetic Resonance

In this section, we will discuss an interesting phenomenon observed in ferromagnetic material called ferromagnetic resonance. As introduced in the previous section, the applied field exerts a torque which causes the magnetization to precess. However, the magnetization precession frequency cannot be described simply by Larmor frequency since it is affected by the various parameters such as magnetic anisotropies, strength and direction of the applied magnetic field, dipolar interaction in case of magnonic crystals, and the macroscopic magnetization of the samples. Applying a time-varying magnetic field having frequency similar to magnetization frequency will excite uniform precession of magnetization. The applied microwave signal is absorbed when the magnetization precession frequency matches with the microwave frequency. This phenomenon is called ferromagnetic resonance [38].

Consider, a ferromagnetic thin film magnetized in x-direction as shown in Fig.2.4(b). A time-varying magnetic field $h(t) = h_y\hat{y} + h_z\hat{z}$ applied causes the magnetization to precess in yz-plane. The dynamic response of the ferromagnet can be studied solving the LLG equation introduced in the previous section. For

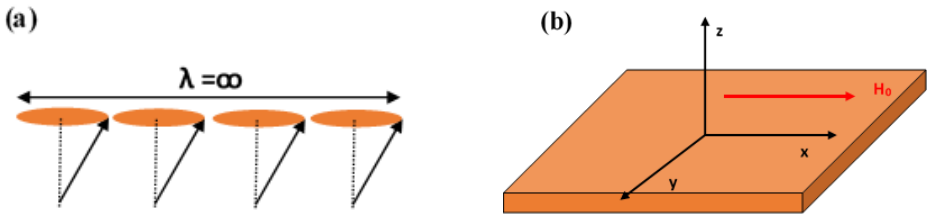

Figure 2.4: (a) Schematic illustrating uniform precession of spins under the influence of time varying magnetic field. (b) Schematic depicting the Cartesian coordinates and direction of applied magnetic field on a sheet representing ferromagnetic thin film.

simplicity, we have neglected the presence of any magnetic anisotropies in the ferromagnet and also have considered ellipsoid geometry of the film to avoid the complex dependence of the demagnetization field on the sample geometry. Considering, $h \ll H_0$ and $m \ll M_S$, the total magnetic field and the magnetization can be written as:

$$H(t) = H_0\hat{x} + h(t) = \begin{pmatrix} H_0 \\ h_y \\ h_z \end{pmatrix} \tag{2.20}$$

$$M(t) = M_S\hat{x} + m(t) = \begin{pmatrix} M_S \\ m_y \\ m_z \end{pmatrix} \tag{2.21}$$

Further, to simplify the problem, we have considered harmonic time variation of magnetization $me^{i\omega t}$ and microwave field $he^{i\omega t}$, where $\omega = 2\pi f$ is the angular frequency. The derivative of m and h is can be given by:

$$\frac{dh}{dt} = i\omega h \quad \& \quad \frac{dm}{dt} = i\omega m \tag{2.22}$$

The effective field inside the ferromagnet is given by the equation:

$$H_{eff} = H_0 - \tilde{N} \cdot M(t) \tag{2.23}$$

Using the value of $\tilde{N}$ from Eq.(2.9)

$$H_{eff} = \begin{pmatrix} H_0 - N_x M_S \\ h_y - N_y m_y \\ h_z - N_z m_z \end{pmatrix} \tag{2.24}$$

The magnetic response to small-amplitude oscillation is given by Polder susceptibility tensor $\tilde{\chi}$. The element of susceptibility tensor $\tilde{\chi}$ can be determined solving

the LLG equation after inserting the values of H(t) and M(t). Since m and h are small, we can neglect the higher-order terms. The solution can be written after introducing news terms $\omega_H = \gamma H_0$, and $\omega_M = \gamma M_S$, in the form:

$$h = \tilde{\chi}^{-1} m \tag{2.25}$$

$$\omega_M \begin{pmatrix} h_y \\ h_z \end{pmatrix} = \begin{pmatrix} \omega_M + \omega_M(N_y - N_x) - i\alpha\omega & -i\omega \\ i\omega & \omega_M + \omega_M(N_z - N_x) - i\alpha\omega \end{pmatrix} \begin{pmatrix} m_x \\ m_y \end{pmatrix} \tag{2.26}$$

The susceptibility tensor $\tilde{\chi}$ can be calculated by inverting the matrix in Eq.(2.26) and can be expressed in the form $m = \tilde{\chi} h$ where $\tilde{\chi}$ is given by:

$$\tilde{\chi} = \begin{pmatrix} \chi_{yy} & i\chi_{yz} \\ -i\chi_{zy} & \chi_{zz} \end{pmatrix} \tag{2.27}$$

where, the matrix elements are given by:

$$\chi_{yy/zz} = \frac{\omega_M \left[\omega_H + (N_{z/y} - N_x)\omega_M - i\alpha\omega\right]}{(\omega_r^2 - \omega^2(1+\alpha^2) - i\omega\alpha \left[2\omega_H + (N_y + N_z - 2N_x)\omega_M\right]} \tag{2.28}$$

$$\chi_{yz/zy} = \frac{\omega\omega_M}{(\omega_r^2 - \omega^2(1+\alpha^2) - i\omega\alpha \left[2\omega_H + (N_y + N_z - 2N_x)\omega_M\right]} \tag{2.29}$$

where, ω_r is resonance frequency, and can be calculated solving the $\det(\tilde{\chi}) = 0$, which gives:

$$\omega_r = \sqrt{\left[\omega_H + (N_y - N_x)\omega_M\right]\left[\omega_H + (N_z - N_x)\omega_M\right]} \tag{2.30}$$

This equation was first derived by Kittel, hence known as Kittel equation. It is evident that the resonance frequency depends on the shape of the ferromagnet through the demagnetization factors. For thin film ($N_x = N_y = 0$, & $N_z = 1$), one can derive the following resonance frequency:

$$\omega_r = \sqrt{\omega_H(\omega_H + \omega_M)} \tag{2.31}$$

The component χ_{yy} which is the largest component of susceptibility will have a dominant contribution to FMR measurements. All the other components χ_{zz},

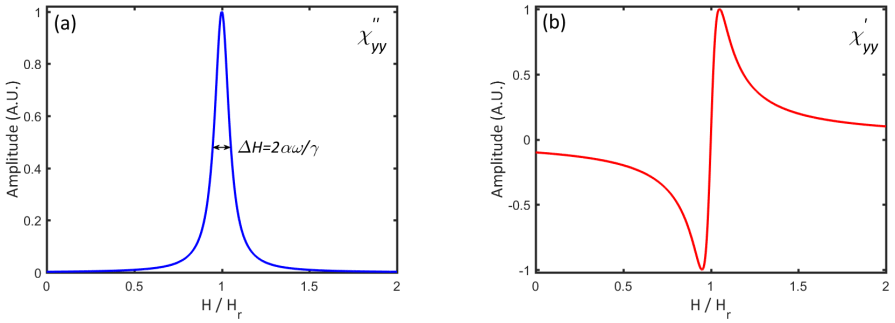

Figure 2.5: (a) The imaginary component of the susceptibility tensor given by Eq.(2.35). (b) The real component of the susceptibility tensor given by Eq.(2.34).

χ_{yz}, and χ_{zy} are small and can be neglected. As evident from Eq.(2.28), susceptibility is a complex function and thus can be separated into real and imaginary components, $\chi_{yy} = \chi'_{yy} + \chi''_{yy}$. For material with very low Gilbert damping ($\alpha^2 \approx 0$), the real and imaginary components are given by the following equations:

$$\chi'_{yy} = \frac{\omega_M \omega_H (\omega_r^2 - \omega^2)}{(\omega_r^2 - \omega^2)^2 + \alpha^2\omega^2(\omega_M + \omega_H)^2} \tag{2.32}$$

$$\chi''_{yy} = \frac{\alpha\omega\omega_H (\omega_H^2 + \omega^2)}{(\omega_r^2 - \omega^2)^2 + \alpha^2\omega^2(\omega_M + \omega_H)^2} \tag{2.33}$$

Since the applied field is considered small compared to the saturation magnetization, $\omega_M > \omega_H$, the above two equation can be further simplified in terms of observables in FMR experiment:

$$\chi'_{yy} = A\frac{(H_0 - H_r)/\Delta H}{(H_0 - H_r)^2 + (\Delta H/2)^2} \tag{2.34}$$

$$\chi''_{yy} = A\frac{1}{(H_0 - H_r)^2 + (\Delta H/2)^2} \tag{2.35}$$

where, A is an amplitude prefactor and $\Delta H = 2\alpha\omega/\gamma$ the linewidth of measured susceptibilities. The imaginary and the real parts are known as symmetric and anti-symmetric Lorentzian lineshape functions shown in Fig.2.5 (a) and Fig.2.5(b) respectively.

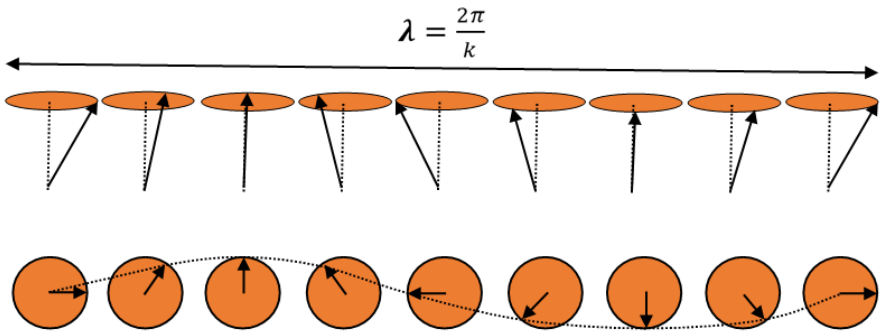

Figure 2.6: Schematic illustrating spin-wave in 1D chain of spins. The precessing spins constitute a wave like disturbance that propagate in the chain, called spin-wave. The wavelength of the spin-wave is given by $\lambda = 2\pi/k$

2.3.4 Spin wave

In the preceding section, we have discussed the uniform precession of magnetization where all the spins precess coherently with the same frequency and the same phase. The excitation can be described as spin-wave with infinite wavelength (i.e. $\lim_{\lambda\to\infty} |k| = \frac{2\pi}{\lambda} = 0$), see Fig.2.4(a). However, when the spins precess with the same frequency but with a finite phase difference between the neighboring spins, the excitation is called non-uniform excitation, see Fig.2.6. Such excitation propagate in ferromagnets and are called spin-wave [32].

Spin waves are low energy excitations in ferromagnets first introduced by Bloch in 1930 in order to explain the temperature dependence of the magnetization [21]. The propagation characteristics of spin-waves are characterized by its frequency-wavevector dispersion. The precession frequency of spin waves differ from that of uniform precession due to the presence of both exchange and dipolar interaction between neighboring spins. Based on these two interactions, spin waves can be categorized into two types. If the tilt angle (the angle at which spins are precessing around their own axis) between the neighboring spins are very small, long-wavelength spin-waves are excited. The contribution of exchange energy to the spin-wave can be neglected. The energy of spin-wave is thus determined by the long-range dipolar interaction, hence regarded as dipolar dominated spin-waves. On the other hand, if the tilt angle is large the exchange interaction cannot be neglected for the resulting short-wavelength spin waves. The spin-wave energy here is mostly governed by exchange interaction and hence referred to as exchange dominated spin waves.

In the following sections, we will provide a general formalism for the spin-waves in ferromagnets. As we have introduced in the previous section, the spins precess with a finite phase difference between the neighboring spin in case of spin-waves ($k\#0$), the exchange energy cannot be neglected. In addition, the dynamic component of magnetization acquires a spatial variation. For small angle precession, the dynamic part of magnetization is given by the sum:

$$m(r,t) = \sum_k m_{k(t)} e^{ikr} \tag{2.36}$$

where, k is spin-wave wavevector and the summation is taken over all the wavevector in reciprocal space.

The exchange energy in this case can be calculated using the Eq.(2.12)

$$\epsilon_{ex} = -A_{ex}\nabla^2 M = -A_{ex}k^2 m(r,t) \tag{2.37}$$

Introducing the exchange energy in the LLG equation, one can obtained the spectrum of dipole-exchange spin-waves. The frequency dispersion of such spin-waves is given by Herring-Kittel formula [39]:

$$\omega = \gamma\sqrt{(H + Dk^2)(H + Dk^2 + 4\pi M_S \sin^2\theta_k)} \tag{2.38}$$

where, $D = \frac{2A_{ex}}{M_S}$ is the exchange stiffness, and θ_k the angle between magnetization and wavevector.

The spin-wave dispersion described by Herring-Kittel formula is only applicable for isotropic and infinite ferromagnetic media. However, a strong anisotropic behavior is observed experimentally in spin-waves with small wavevector. The discrepancy arises because of the fact that the dynamic magnetization generates stray field through Maxwell'magnetostatic equations which were not considered in the solution. Taking this into account, R. W. Damon and J. R. Eshbach [40] gave solution for two types of spin-waves in in-plane magnetized thin films - magnetostatic surface waves and magnetostatic volume waves

The dispersion relation for spin-waves taking the additional stray and dipolar field into account is given by Kalinikos and Slavin [41]:

$$\omega = \gamma\sqrt{(H + Dk^2)(H + Dk^2 + 4\pi M_S F_{pp}(k_p))} \tag{2.39}$$

where, $F_{pp}(k_p)$ is the matrix element of the dipole-dipole interaction given by:

$$F_{pp}(k_\rho) = 1 + P_{pp}(k)[1 - P_{pp}(k)]\frac{M_S}{(H + Dk^2)}\sin^2\theta_k - P_{pp}(k)\cos^2\theta_k \tag{2.40}$$

where, the wavevector $k = \sqrt{k_\zeta^2 + k_\rho^2}$, k_ζ and k_ρ, (where,$k_p = \frac{\pi p}{d}, p = 0, 1, 2$) are in-plane and out-of-plane component of the wavevector. The in-plane wavevector further has two components - $k_\parallel$ and $k_\perp$, parallel and perpendicular to the magnetic field respectively. The function $P_{pp}(k)$ is given by:

$$P_{pp}(k) = 1 - \frac{(1 - e^{-kd})}{kd} \tag{2.41}$$

Now we will consider the dispersion Eq.(2.39) for the spin-waves in special geometry. For the case of magnetostatic spin-waves, the exchange energy term can be neglected. The dispersion curve for spin-wave propagating perpendicular to magnetization $(k \perp M)$ is given by:

$$\omega_{DE} = \gamma \sqrt{H(H + 4M_S) + (4\pi M_S)^2 \left(\frac{(1 - e^{-2k_\perp d}}{4} \right)} \tag{2.42}$$

This spin-wave is called magnetostatic surface wave (MSSW) also known as Damon Eshbach (DE) wave named after the scientists who discovered it. Fig.2.7 illustrates the MSSW spin-wave. The amplitude of dynamic component of magnetization for such spin-wave reaches maximum at the surface and decay exponentially within the film. This spin-wave possesses positive group velocity since the frequency of the wave increases with increasing wave vector, see Fig.2.10(a).

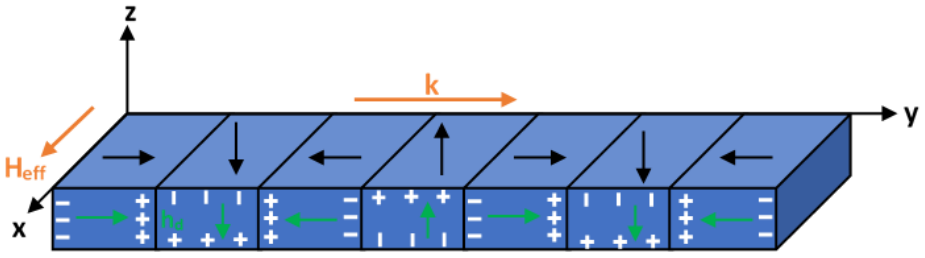

Figure 2.7: Sketch illustrating the propagation of magnetostatic surface spin-wave. The black arrows show the precession of dynamic component of the magnetization as the wave propagates [42].

The dispersion relation for the spin-wave propagating along the same direction as the applied field is given by:

$$\omega_{MSBVW} = \gamma \sqrt{H \left(H + 4\pi M_S \left(\frac{1 - e^{-k_\parallel d}}{k_\parallel d} \right) \right)} \tag{2.43}$$

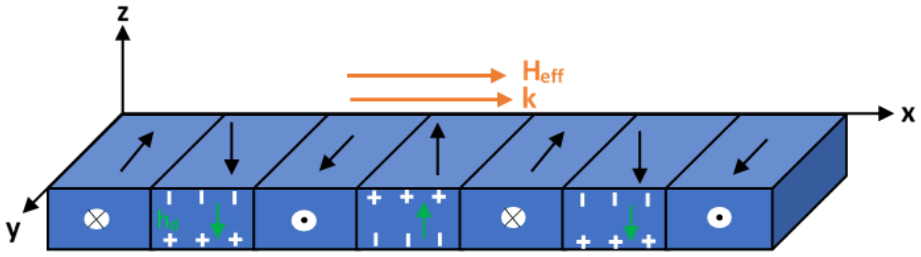

Figure 2.8: Sketch illustrating the propagation of magnetostatic backward volume wave. The black arrows show the precession of dynamic component of the magnetization as the wave propagates [42].

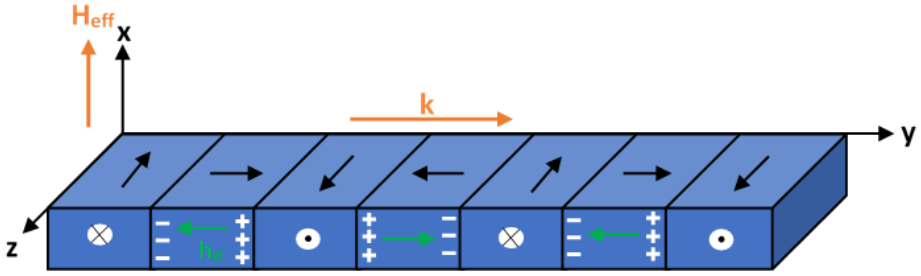

Figure 2.9: Sketch illustrating the propagation of magnetostatic forward volume wave. The black arrows show the precession of dynamic component of the magnetization as the wave propagates [42].

The spin-wave is called magnetostatic backward volume wave (MSBVW). Fig.2.8 illustrates the precession of the dynamical component of magnetization. The frequency of the mode decreases with increasing wave vector and thus this mode owns negative group velocity, see Fig.2.10(b).

For the case of magnetic field applied perpendicular to the film plane, the dispersion relation of the spin-wave is given by:

$$\omega_{MSFVW} = \gamma\sqrt{H\left(H + 4\pi M_S\left(1 - \frac{1 - e^{-k_\varsigma d}}{k_\varsigma d}\right)\right)} \tag{2.44}$$

Such excitation is called magnetostatic forward volume wave (MSFVW), illustrated in Fig.2.9. The dispersion curve of the spin-wave does not depend on the direction of in-plane wave vector (k_ς), see Fig.2.10(c).

For the case of exchange dominated wave or thickness or perpendicular standing spin-waves (PSSW), the term for dipole-dipole interaction can be neglected and the dispersion curve is given by:

$$\omega_{PSSW} = \gamma\sqrt{\left(H + Dk_{\|}{}^2 + D\left(\frac{\pi p}{d}\right)^2\right)\left(H + Dk_{\|}^2 + D\left(\frac{\pi p}{d}\right)^2 + 4\pi M_S\right)} \tag{2.45}$$

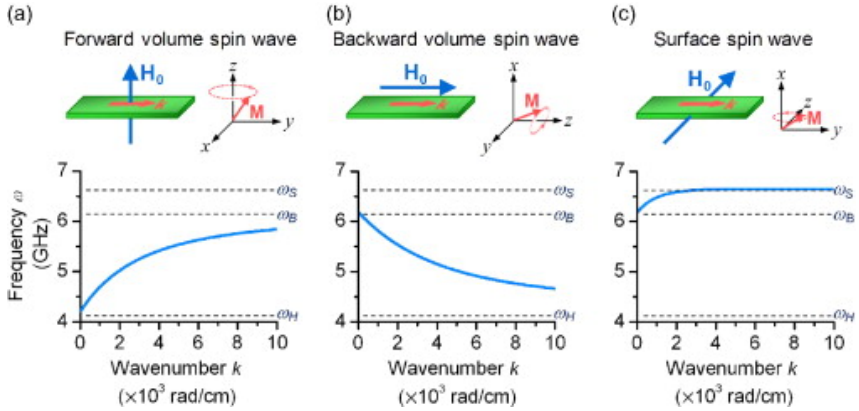

Figure 2.10: Schematics depicting the film/field configuration, magnetization precession (on the top) and frequency-wavevector dispersion (on the bottom) for the MSFVW, MSBVW, and MSSW in a long and narrow magnetic thin-film strip in **(a)**, **(b)**, and **(c)** respectively [43].

2.3.5 Magnetization relaxation

As we have introduced before, the external applied field exerts a torque on the magnetization which causes the magnetization to precess around the effective field. The magnetization precession damped over time and finally get relaxed along the effective field. The magnetization relaxation is caused by dissipation of energy from the spin to the lattice. The phenomenological Gilbert damping parameter (α) was introduced in LLG Eq.(2.19) in order to take the dissipation into account. The energy dissipation can occur directly or indirectly through many interaction channels such as electron-magnon interaction, spin-spin interaction and due to scattering from the surface or impurities in the material [44]. These damping processes are generally categorized into two - intrinsic and extrinsic [45].

The damping parameter α is experimentally measured from the full linewidth at half maximum (FWHM) of the imaginary part of the Polder susceptibility tensor. Fig.2.11 shows the FMR linewidth measured as a function of frequency for the

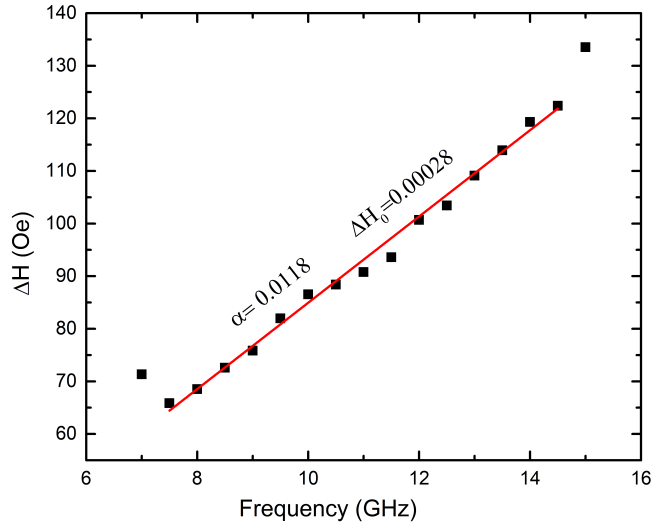

Figure 2.11: An example of the FMR linewidth plotted against microwave frequency. The experimental data is fitted to the Eq.(2.46). The slope and intercept of the fitted line give Gilbert damping parameter,α and inhomogeneous linewidth, ΔH_0

Permalloy magnonic crystals. In conventional field sweep FMR, the linewidth is generally measured in terms of field which consists of a frequency-dependent term and a term independent of frequency given by the relation [46]:

$$\Delta H = \Delta H_0 + \frac{4\pi}{\gamma}\alpha f \tag{2.46}$$

The slope of the Eq.(2.46) gives the Gilbert damping parameter (α) and the intercept gives the frequency independent damping also called inhomogeneous line broadening. The intrinsic Gilbert damping is caused by spin-orbit coupling since this process does not conserve spin [47]. However, there are several other mechanisms such as two magnon scattering, spin transfer torque (STT), and inhomogeneous line broadening which also contribute the FMR linewidth in addition to the intrinsic Gilbert damping [32].

In following section, we will discuss the various intrinsic and extrinsic processes contributing to the FMR linewidth.

Two magnon scattering

The two magnon scattering is a process through which energy is dissipated from FMR mode to degenerate magnons over a range of wave vectors [48]. The energy absorbed by the uniform mode from the microwave field dissipates to the lattice via scattering to the degenerate magnons in the system. The degenerate magnons don't couple to the microwave field and thus generally not excited. Since this process involves magnons having the same energy but different wavevectors, the momentum is not conserved. Therefore, inhomogeneity or impurity which serves to conserve angular momentum is required for this process to happen.

Theoretical model describing two magnon scattering can be given by the formalism of second quantization according to which FMR mode is destroyed to create spin-wave mode of the same energy. The scattering rate for a transition from a magnon at state $k = 0$ to state $k\#0$ can be given by Fermi golden rule [48, 49]:

$$\Gamma = \frac{2\pi}{h} \sum_{k} |F_k|^2 \delta(h\omega_k - h\omega_0) \tag{2.47}$$

where, h is Planck'constant, $\delta(h\omega_k - h\omega_0)$ is the Dirac delta function. The factor $|F_k|^2$ represents the probability of scattering or coupling of FMR mode to spin-wave modes.

The Eq.(2.47) points out that the scattering rate from uniform mode to degenerate magnon mode is dependent on the final magnon state available into. Thus, the scattering rate can be suppressed by reducing the number of degenerate magnon states available for scattering. For the in-plane ferromagnetic resonances, there are several magnon states degenerate to the uniform mode and thus result in a significant contribution of two magnon scattering to the linewidth. Tilting the magnetization from in-plane to out-of-plane, one can effectively reduce the degenerate magnon states. When the magnetization is fully out-of-plane, no degenerate magnons remains available and thus no scattering. Therefore, the two magnon scattering can be totally suppressed.

In-homogeneous linewidth

Inhomogeneous linewidth broadening comes from the in-homogeneities in the ferromagnet. This in-homogeneities could be spatial variation in the sample magnetization, magnetic anisotropies etc. These sources cause local variation in effective magnetic field inside the ferromagnet. Thus, the region with different effective field will fulfill resonance condition locally. The observed ferromagnetic resonance is the superposition of all these local resonances apparently with enhanced linewidth.

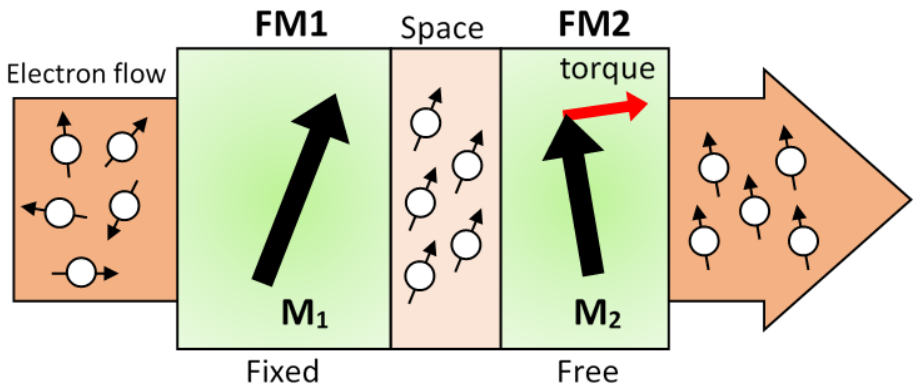

Figure 2.12: Schematic illustrating spin transfer torque. Charge current flowing from left to right first gets polarized by the fixed FM1 layer which further exerts toque on FM2 transferring their angular momentum

2.3.6 Spin transfer torque

As we know, the electron carries both charge and spin degree of freedom. The spins in the charge current flowing through a non-ferromagnetic electronic device are randomly oriented and do not play a significant role in the device performance. However, the transport become polarized when ferromagnetic material is incorporated in the device. The electrons whose spin orientation matches with the magnetization direction passes easily through the layer, rest suffer scattering. The flow of such polarized current is called spin current [50].

The current flowing in the spintronics device does not merely respond to the layer magnetization but also disturbs it. This was first predicted by Slonczewski and Berger in 1996 in magnetic multilayers [9, 10]. They observed a transfer of spin angular momentum between the spin current and the ferromagnetic layer. This effect is known as Spin Transfer Torque. Fig.2.12 depicts the basic concept of the spin transfer torque in two ferromagnets separated by spacer.

The STT can be effectively used for magnetization reversal. This concept gives birth to a new device technology called spin transfer torque magnetic random-access memory (STT-MRAM) [2, 12]. The STT-MRAMs are much faster, efficient and easier to scale-down compared to toggle MRAM. In STT-MRAM, data are recorded in tiny ferromagnetic layers aligned either parallel or opposite to the permanently magnetized base layer. The data bits are read by measuring the change in resistance of the circuit passing a current through it. However, the high cur-

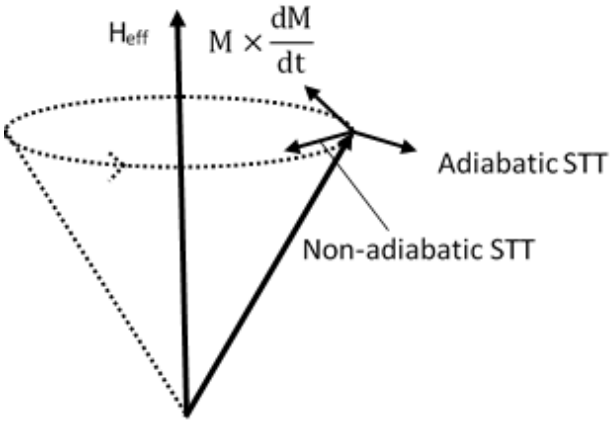

Figure 2.13: Sketch illustrating magetization (M) precession under the influence of effective magnetic field H_{eff}. The current induced adiabatic and non-adiabatic torques are shown in the black arrows.

rent density can generate torque enough for switching the magnetization of the upper layer and provides a way of writing and rewriting MRAM data. The current induced spin transfer torque can also make magnetization to precess whose precession frequency can be controlled by the applied current. This concept has been demonstrated in microwave oscillators such as spin torque oscillator [13].

The current induced STT is also important in the system where the magnetization is not uniform but gradually changing its direction such as domain-walls and spin-waves. In the adiabatic limit where a full transfer of angular momentum to local magnetization is applied. The adiabatic STT in such a system is given by [51]:

$$\tau_{adia} = -(u \cdot \nabla)M \tag{2.48}$$

where, u is the velocity vector directed along the motion of the electron with the amplitude:

$$u = g\mu_B \left(\frac{JP}{2eM_S}\right) \tag{2.49}$$

where, g is Lande g-factor, μ_B the Bohr magnetron, J the current density, P the polarization.

A toque perpendicular to the torque given in Eq.(2.48) also exits known as non-adiabatic spin transfer torque or field like torque given by:

$$\tau_{non-adia} = \beta\left[u \cdot (M \times \nabla)\right] M \tag{2.50}$$

where, β is non-adiabaticity parameter.

The LLG equation in presence of spin current is modified to:

$$\frac{dM}{dt} = -\gamma M \times H_{eff} + \frac{\alpha}{M_S}\left[M \times \frac{dM}{dt}\right] - (u \cdot \nabla)M + \beta\left[u \cdot (M \times \nabla)\right] M \quad (2.51)$$

2.4 Micromagnetic simulations

Micromagnetics is a branch of physics that deals with the dynamic behavior of the magnetic materials on a length scale large enough for the atomistic model of material to be ignored (continuum approximation) and small enough to resolve the magnetic structures such as domain walls. In micromagnetics, the small angle precession of spins is considered so that the angles of the spin's direction can be approximated by a continuous function of position. The magnetization of the ferromagnets is represented by the continuous vector field, $M = M_s m$, where M_s is the saturation magnetization and m the local direction of magnetic spin. Micromagnetism is a semiclassical theory which utilizes quantum mechanical effect in the framework of classical field theory [35].

The purpose of micromagnetics is to determine the spatial distribution of local magnetization. It was first used to calculate the equilibrium position of magnetization by minimizing the total magnetic energy in the system. Micromagnetism emerged as a standard tool for analyzing basic magnetic properties in ferromagnets in micro and nanoscales after a report of Landau-Lifshitz's wall calculations and Brown's micromagnetic equations. Currently, it's being used in solving static and dynamic problems in ferromagnets [35].

For the work done in paper II of this thesis, we used MuMax3 [52] micromagnetic simulations employing finite difference discretization to solve the LLG equation. The simulations are performed dividing the magnetized region of the space into small cells. When dividing the cells, it is important to consider the length of the cell less than or equal to the exchange length. The spins of the magnetized ferromagnet are assigned at the center of these cells. The coupling is considered at the faces between the cells. The micromagnetic solver then solves the LLG equation numerically assuming the magnetization as a continuous function of the space.

Chapter 3

Model material systems

In this section, a brief overview of the research field and a comprehensive literature review of the materials used to perform the work in this thesis is presented. The aim is to establish a context for the work presented in this thesis.

Spin dynamics in ferromagnets is among the most active research topic in magnetism. Especially the ferromagnets with low magnetic damping have attracted considerable attention of the science community for their potential application in spintronic and magnonic devices [2, 20]. Magnonics is an emerging field in the condensed matter physics that deals with magnetic phenomena related to spin-wave in the nano-structure of ferromagnets. Magnonics aims at excitation, detection and manipulation of spin-waves for their successful application in information and data processing. The damping of the material limits the distance over which the information can be carried. The magnetic damping is thus the key parameter deciding the functionality of the material in devices. Hence, the material with small Gilbert damping compatible with CMOS technology is of utmost importance for magnonics device applications.

Permalloy is a metallic ferromagnet first discovered in 1914 by Gustav Elmen at Bell Telephone Laboratories. Many decades after its discovery, it has attracted a lot of attention of the science community when reported to have low Gilbert damping. It is a prototype material known for the lowest Gilbert damping parameter ($\alpha \approx 0.001$) among the metallic ferromagnets [53]. The low magnetic damping in combination with high Curie temperature (T_C=553K) as well as its compatibility with CMOS technology makes it potential candidates for applications in spintronics devices. The spin waves which are building block of the magnonics have been widely studied in permalloy both for their interesting underlying physics as well

as for their potential technological applications [54–60]. One of the main interests is how to control and manipulate spin waves making it facile for devices. The magnonic crystals offer a promising way to control and manipulate spin waves in ferromagnets [30, 61–63]. Therefore, exploring and understanding spin waves in MCs are important for the application in spintronics devices.

Magnonic crystals (MCs) are meta-materials with the periodic variation in magnetic properties in space. The MCs are the magnetic counterpart of photonic crystals which are well known for molding the electromagnetic wave [64]. The same idea is transferred to ferromagnets to manipulate the spin waves. The periodic variation in magnetic properties could be due to modulation of saturation magnetization realized by ion implantation, modulation of magnetic anisotropy, periodic modulation of ferromagnetic stripes or dot on dielectric or ferromagnet substrate, periodic perturbation of the magnetic field or any other modulating parameter modifying the propagation of spin waves [65–70]. The periodic modulation brings a change in magnetostatic (e.g. induced magnetic anisotropy, change in the coercive field) and magnetodynamic (e.g. spin-wave localization, collective excitation of spins) properties significantly [71, 72].

MCs find applications in wide range of spin wave devices e.g. advanced magnetic storage, data storage and spin logic gates [29, 30, 73]. Depending on design of MCs, the spin wave forms a band of quantized or localized modes due lateral confinement and sometimes band gaps when the spin wave wavelength is longer and shorter than the period of the modulation respectively [62]. Owing to their interesting underling physics and wide range of potential applications, the static and dynamic properties of MCs have been studied extensively in one dimension, two dimension and three dimensions both experimentally and theoretically [72, 74–76].

1D MCs have attracted considerable attention because of their simple geometry convenient for studying the impact of geometry confinement on the magnetodynamic properties. Especially the MCs with large length to width ratio making it possible to eliminate the effect of non-homogeneity due to the demagnetization field when magnetized along the long direction of MCs [72, 75, 77]. This geometry also makes easy to study the impact of dipolar interaction on the magnetodynamic properties. Advances in lithography technique make it possible to fabricate MCs with small lateral confinement where the static field from the neighboring elements interferes which results in formation dipolarly coupled MCs [78, 79]. Under the magnetic resonance condition, the dynamic component of magnetization precessing at the edge of magnetic stripe couples with the neighboring stripes through the dipolar interaction and form a collective spin excitation in system [80, 81]. Such excitation results in magnonics band formation whose bang gap is tunable by the

control parameter of the MCs. The dipolar coupling when large enough can also be used to tailor the magnetodynamic properties. However, a detailed investigation regarding the impact of inter-lattice separation on the magnetodynamic properties is still missing which is one of the main objectives of this thesis.

Complex metal oxides are known for their fascinating electronic and magnetic properties. The complex correlation of charge, spin and orbital degree of freedom in these material result in emergent phenomenon such as high temperature superconductivity in cuprates, ferroelectricity, metal-insulator transition and colossal magnetoresistance in manganites [82–84]. In addition to these bulk effects, the interfaces at complex oxide heterostructure are also promising for the novel physical properties emerging from structural, electronic and orbital reconstructions [83, 84].

Mixed valanced manganites have attracted huge attention because of their colossal magnetoresistance and high degree of spin polarization [85, 86]. The High colossal magnetoresiatance (CMR) makes it attractive candidate for the electrode material in magnetic tunnel junctions (TMJs) [87]. Within manganites, $La_{0.7}Sr_{0.3}MnO_3$ (LSMO) is ferromagnetic half-metal at room temperature and known to have highest Curie temperature (T_C=370K) among all the manganites [88, 89]. These unique properties makes it potential candidates for technological applications. Scientific advances in past few decades has successfully demonstrated excellent device functionalities of LSMO in spintronics devices [89–92]. The low Gilbert damping parameter ($\alpha \approx 0.002$) reported makes this material also an attractive candidate for magnonics devices [93]. However, it is extremely difficult to grow LSMO with abrupt interfaces which is required for device applications. Thanks to pulsed laser deposition technique which allows growth of atomically sharp epitaxial LSMO interface on $SrTiO_3$ (STO) substrate [94, 95]. Transport and static magnetic of LSMO grown on various orientations of STO has been studied widely. However, less attention has been paid on its magnetodynamic properties.

The LSMO/STO heterostructure interface has been studied widely for their interface induced emergent phenomenon ascribed to orbital and spin reconstructions [96]. The induced ferromagnetism at such interfaces are of primary importance since it provides new prospects for the 2D spintronics at interface [97]. The (111) oriented LSMO/STO heterostructure interfaces are interesting in this regard because of terminating polar layer which is more prone to the orbital and spin reconstructions. The investigating magnetodynamic properties at such interface is important for understanding the underlying physics as well as for the potential applications in spintronics devices.

Heusler alloy with stoichiometric composition X_2YZ, where X and Y are

transition metals and Z is p-block element, has been studied extensively because of its half metallicity and low Gilbert damping [26, 98, 99]. Among the numerous Heusler alloy, Co_2FeAl (CFA) is famous for its high Curie temperature (T_C= 1000 K), high degree of spin polarization, and low Gilbert damping $(\alpha \approx 0.001)$ [100, 101]. Its compatibility with CMOS technology makes it interesting for both spintronics and magnonics applications. Investigations previously done on CFA have been focused on its static and magneto-dynamic properties where its high magnetoresistance and low Gilbert damping for the potential applications in magnetic tunnel junctions and STT based MRAM devices have been demonstrated [102–105]. However, investigation of spin-waves propagation properties and its dependence on spin-wave frequency are still missing.

Chapter 4

Experimental techniques

This chapter will give the reader a detailed information of the main experimental techniques used for sample growth as well as the techniques utilized for sample characterization.

The Permalloy MCs presented in paper II were grown by electron beam evaporation. The spin-wave device used for developing propagating spin-wave spectroscopy and investigating spin-wave propagation properties in Permalloy and Heusler alloy thin films presented paper III and paper IV were grown by a combination of DC magnetron sputtering and electron beam evaporation techniques. The magnetodynamic properties of the complex magnetic oxide and MCs presented in paper I and II were investigated by cavity and broadband FMR techniques. The propagation properties of the spin-wave were studied by propagating spin-wave spectroscopy presented in next chapter.

4.1 Physical vapor deposition

Physical vapor deposition (PVD) is a process of depositing thin films or coating by evaporating a solid target material to the vapor phase and then back to solid-phase on the desired substrate in low-pressure chamber [106]. The PVD method can be categorized mainly into two groups. The first which involves evaporating the material by heating is called thermal vapor deposition. And the second which involves material deposition by argon plasma is called sputtering.

AJA international custom made e-beam evaporator and sputter coater was used for the thin film deposition. A brief introduction of the techniques involved will be given in the following section.

4.1.1 DC magnetron sputtering

Sputtering is a plasma vapor deposition technique primarily used for thin film deposition [106]. A very high voltage is applied between two electrodes (target and the substrate) placed in a high vacuum chamber. The applied voltage ionizes the argon atoms when pursed in the chamber. The ionized Ar^+ atoms get accelerated and strike the target. While doing so they knock out the material which settles down on the substrate. In magnetron sputtering, a magnetic field is applied in addition to the electric field which confines plasma close to the target and enhances the ionization efficiency and thus helps in getting plasma at lower pressure. This technique has primarily two variants based on the voltage source used. The first one is DC magnetron sputtering, where a DC voltage source is used for generating the plasma. The DC voltage source suits best for conducting targets. The second one is RF magnetron sputtering, where rf source is used for depositing insulating materials. Fig.4.1 shows the schematic of the DC magnetron sputtering technique.

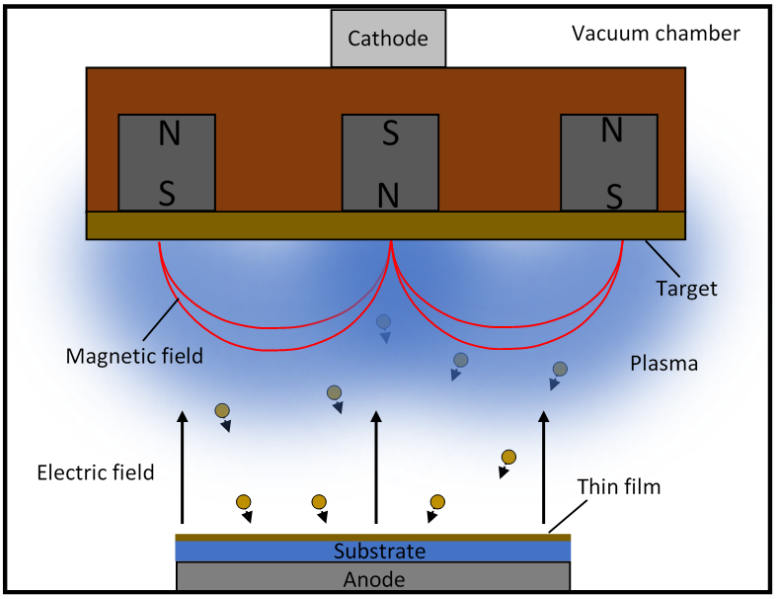

Figure 4.1: Schematic depicting the thin-film deposition by DC magnetron sputtering.

4.1.2 Electron beam evaporator

Electron beam evaporation is another type of physical vapor deposition technique also widely used for coating and thin film depositions. The target material to be deposited is heated by an electron beam source emitted from a charged tungsten

filament. The target material transforms into gaseous phase which get deposited on the substrate [106]. The high vacuum in the chamber provides a very large mean free path to the evaporated particles which result in a very smooth and uniform deposition. Fig.4.2 shows the schematic of electron beam evaporation set up. The growth rate was monitored by a quartz crystal. A rotation stage which ensures the good homogeneity of the deposited material is used during the growth.

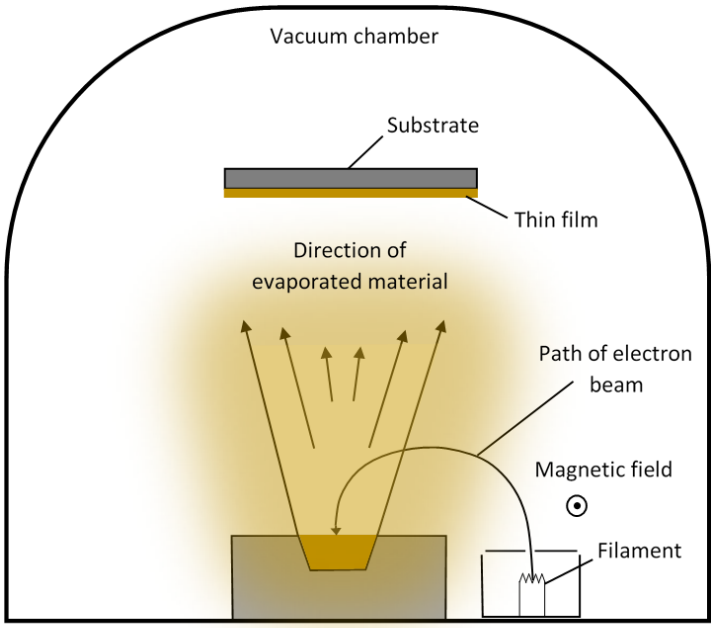

Figure 4.2: Schematic illustrating deposition of thin film by electron beam evaporation setup

4.2 Electron beam lithography

Electron beam lithography (EBL) is an advanced lithography technique widely used for nano-patterning. In principle, this technique is similar to photolithography where accelerating electron beams are used to exposed electron sensitive resist in contrast to UV-radiation in photolithography. This is one of the best lithography techniques which provides sub-10 nm resolution. The accelerated electron beam is scanned across the sample in order to expose the resist, therefore it does not require any hard mask. However, it takes a long time to expose the resist.

ELIONIX ELS-G100, an electron beam lithography machine with 100 keV

electron gun was used for the work performed in the thesis. The electron beam current in the range of 1nA-100pA were used for resist exposure. The beam spot size varies accordingly with the beam current with minimum diameter of 1.8 nm at 100 pA. The exposure time which is given by *time(t) =Dose (D)* $\times$ *Area (A)/beam current (I)* can be selectively reduced by choosing optimum beam current for the given feature size.

Once an appropriate beam current is chosen for a given feature size, exposure dose must be optimized. If the dose is too low (high), the resist will be under-exposed (overexposed) which results in broken or swelled features after liftoff. A positive tone e-beam resist, AR-P 6200 (CSAR62) was used for the work performed in this thesis. The exposure dose was optimized for the different beam current used in the exposure.

4.2.1 Proximity effect correction

The electron beam when interacts with the matter (resist), many types of the secondary beam are generated. The primary electron while passing through the resist suffers multiple scattering. The scattered electrons re-exposes the resist and thus can over-expose the resist. The low energy secondary electrons which are generated because of in-elastic scattering within resist do not play a significant role as they die-off traveling few nanometers. However, backscattered electrons possess energy high enough to travel a long distance and can over-expose the resist. These electrons scattering effect is called proximity effect. There is a huge impact of the proximity effect on pattern quality when exposing patterns containing small as well as large feature size. The process often fails due to the large variation in the optimum dose required for these patterns. Hence, proximity effect correction became necessary when exposing such patterns in a single layer. A software called BEAMER developed by GenISys has been used to make an exposure file for electron beam lithography [107]. This software employs a simulation model for various resists type and thickness on different substrates. The software divides the whole pattern into bulk and sleeve parts and assigns different doses to them. This also helps in reducing the total exposure time which is a major issue with electron beam lithography. Fig.4.3 shows an exposure file defined after dose correction using BEAMER software. The color contrast shows the dose difference between the various part of the pattern. The bulk patterns (bluish region) generally required less dose compared to the smaller one (greenish region).

4.3 Ion beam etching

Ion beam etching (IBE) is a physical dry plasma etching technique used for removing material from the substrate. This technique utilizes the neutral /reactive

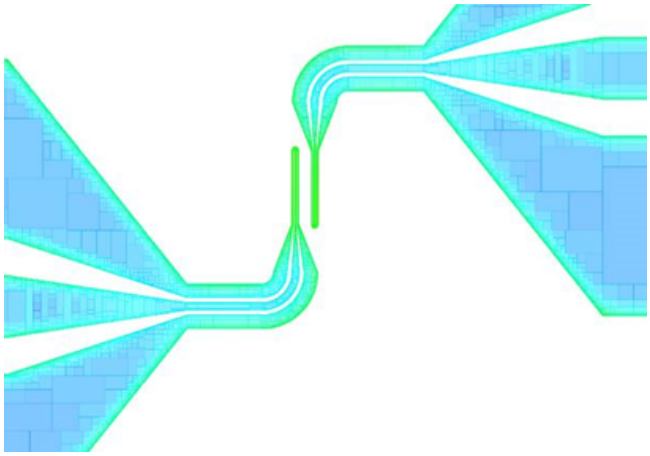

Figure 4.3: An image depicting an exposure file made by BEAMER software. The color contrast shows the different dose assigned to various part of the pattern.

ions and accelerates them towards the sample in a very controlled fashion. Ion beam etching is regarded as a universal etchant method because of its applicability for a wide range of materials with excellent etch rate, selectivity and uniformity. IBE consists of three mains parts: discharge chamber, grids and neutralizer. Ions are produced in the discharge chamber injecting gas like argon in RF-field. The RF-field applied in the discharge chamber excites free electron. When the free electrons acquire enough energy, they start breaking argon atoms into ions and plasma is created in the chamber. The potential grids then come into play whose role are basically to extract and accelerate the ions toward the substrate. The grids are two or three in numbers and are kept at different potentials. The grid which remains in electric contact with the plasma is kept at positive potential relative to the ground and is called screen grids. Its function is to screen the ions coming out of the discharge chamber and thus it controls the beam voltage or energy. A second grid that is kept at negative potential relative to the ground is called the accelerator grid provides extraction voltage to the ions. A third grid called decelerator is grounded and helps to reduce the beam divergence and avoid re-deposition of sputtered material back on the accelerator grid. The filament is placed in between the sample and the accelerating grid which produces electrons by ionizing argon atom. The third part (neutralizer) which is basically a filament serves to avoid charge build-up and to neutralize some of the ions to balance the beam [108].

The ion beam etching are generally categorized into types: ion beam etching (IBE), reactive ion beam etching (RIBE) and chemically assisted ion beam etching

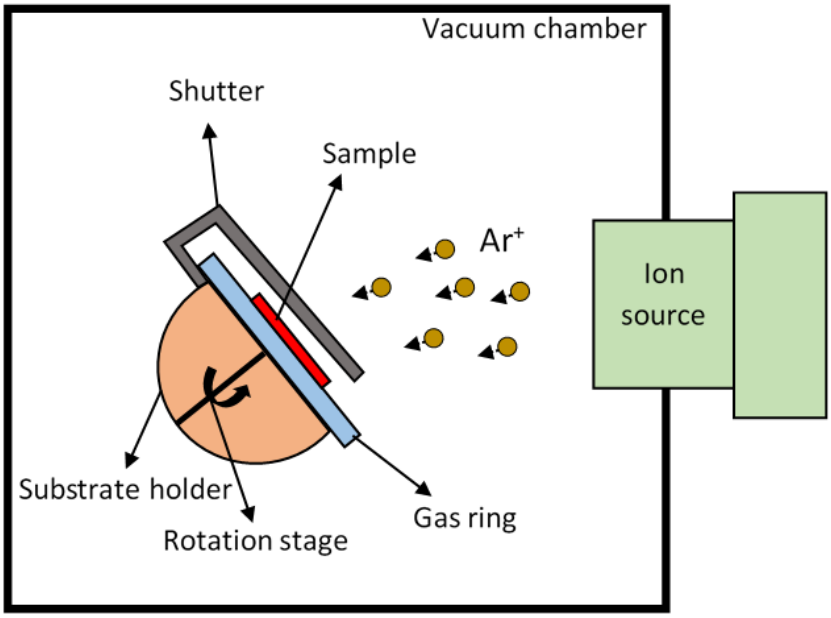

Figure 4.4: Schematic depicting chemically assisted ion beam etching set up.

(CAIBE). All these variant works on the same principle, the differences lie on the combination of etchant ions used.

4.3.1 Chemically assisted ion beam etching

Chemically assisted ion beam etching (CAIBE) is a type of ion beam etching where chemically active gases such as O_2, SF_6, CHF_3, Cl_2 are used in addition to neutral etchant gas e.g Ar. The reactive gases are introduced near the substrate holder around the wafer through a gas ring which helps in improving the etch rate and the selectivity of the mask.

Ionfab 300 Plus, an Oxford instrument was used for defining the magnetic strips for spin-wave device fabrication. Fig.4.4 shows the schematic of the CAIBE setup. The sample is attached to a 4-inch loading wafer with the help of Kapton tape. The wafer is then transferred to the substrate holder which is connected to a rotation stage in the ion beam chamber. The etching is performed with rotation stage tilted at 60 degrees for the desired time and finally for 1 min with the tilt angle of 10 degrees, which helps to remove the side walls deposition during the course of the etching process. The beam current, beam voltage and accelerating voltage were kept at 500 mA, 500V and 300V respectively. The Ar and O_2 flow

rate was fixed at 10 and 5 sccm respectively.

4.4 FMR spectroscopy

Ferromagnetic resonance spectroscopy is a very sensitive nondestructive tool widely used for probing magnetic materials. This allows investigating static and magnetodynamic properties of ferromagnets such as magnetic anisotropies, effective magnetization and magnetic damping.

This technique works on the principle of Ferromagnetic Resonance introduced in the previous chapter. The applied static magnetic field magnetized the ferromagnet along its direction. The microwave field then applied to excite the uniform precession of magnetization whose frequency depends on the effective magnetic field in the ferromagnet. When the processional frequency matches the microwave frequency, the resonance condition is fulfilled, and the signal is absorbed. The resonance condition can be fulfilled by two ways either sweeping the applied magnetic field or sweeping the microwave frequency. The absorbed signal which contains detailed information about the ferromagnets is recorded and analyzed to extract the magnetic properties.

For the work presented in this thesis, two complementary field-sweep FMR techniques have been used. In the following section, the two FMR techniques will be introduced.

4.4.1 Cavity-based FMR

The cavity FMR measurements were carried out in a commercial X-band electron paramagnetic resonance (EPR) setup with a fixed microwave frequency of 9.4 GHz (Bruker Bio-spin ELEXSYS 500, with a cylindrical TE-011 microwave cavity). The schematic of the setup is shown in Fig.4.5. The set up consists of three main components - a microwave wave bridge, an electromagnet capable of providing a magnetic field up to 8000 Oe, and a microwave cavity. The microwave wave bridge houses the solid-state microwave source, a circulator and a detector. The bridge is connected to the microwave wave cavity through an impedance matched rectangular waveguide for optimal coupling. The sample is attached to a cylindrical quartz rod and placed at the center of the cavity. The quartz rod is connected to a goniometer allowing to rotate the sample 360° in-plane as well out-of-plane.

To record the FMR absorption, we first apply a static magnetic field perpendicular to the applied microwave field. The magnetic field is then swept to fulfill the ferromagnetic resonance condition. At resonance, when the magnetization processional frequency matches with microwave frequency, the microwave signal is absorbed. The absorption is recorded by measuring the change in reflected power

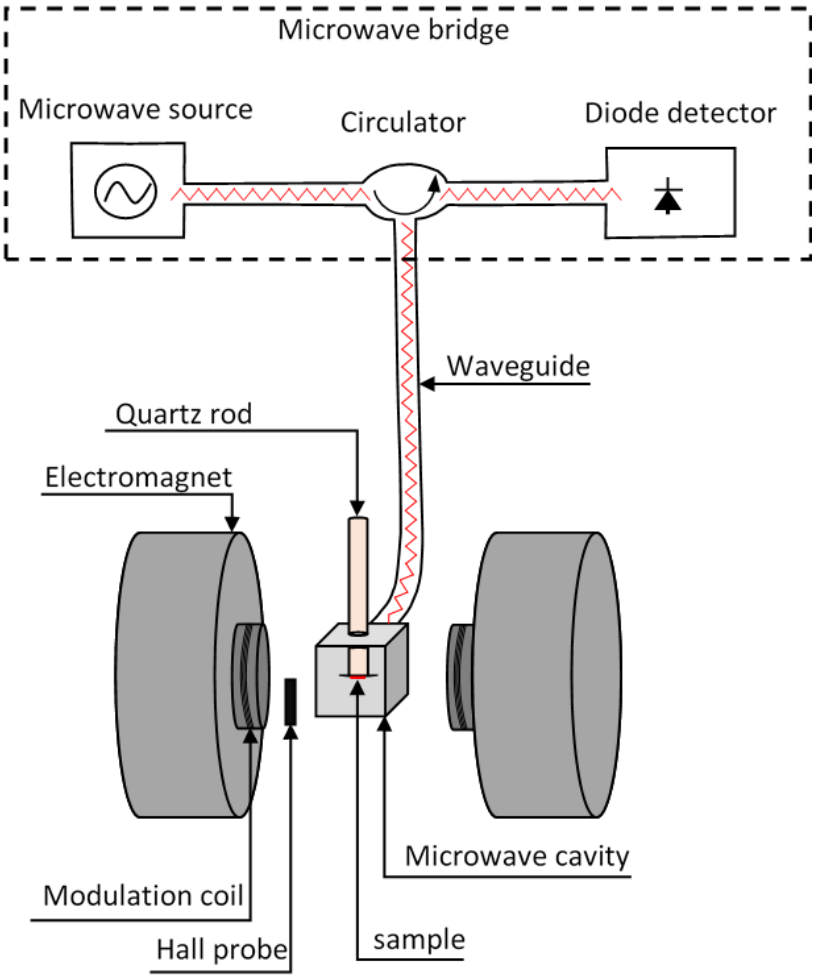

Figure 4.5: Schematic illustrating cavity FMR setup.

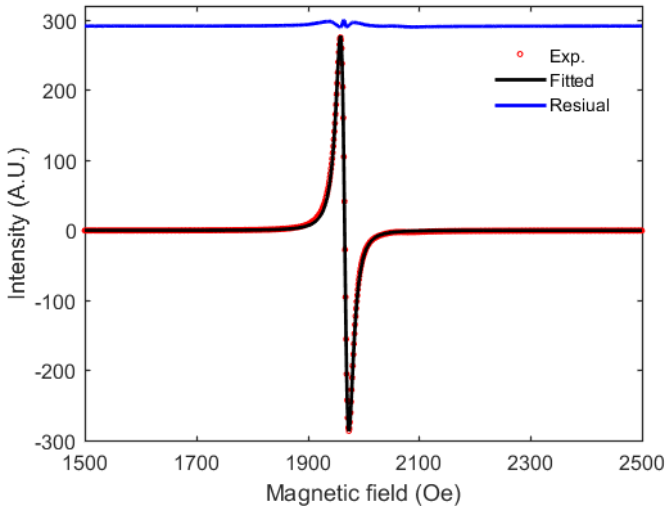

Figure 4.6: The FMR lineshape measured on 15 nm LSMO/STO(111) sample employing cavity FMR technique.

by the detector in the microwave bridge.

As introduced before, the recorded absorption curve is proportional to the imaginary part of the susceptibility tensor. The FMR absorption signal is generally described by the sum of symmetric and antisymmetric Lorentzian function given by:

$$\chi'' = A\frac{1 + (H_R - H_0)/\Delta H}{(H_R - H_0)^2 + (\Delta H/2)^2} \tag{4.1}$$

where, A is a pre-amplitude factor, β asymmetry parameter defining the asymmetry of lineshape, ΔH the full width at half maximum (FWHM), H_R and H_0 are the resonance field and the applied magnetic field respectively. The antisymmetric Lorentzian part arises due to the phase difference between the electric and magnetic field of microwave in the cavity [109].

The setup is equipped with field modulation technique to enhance the sensitivity of measurement. The measurements were performed under small modulation field, therefore, the measured FMR signal is proportional to first field derivative of the susceptibility tensor. The experimental FMR lineshape recorded is thus fitted to the derivative of Eq.(4.1) given by:

$$\frac{(d\chi'')}{dH_0} = A\left[\frac{-\beta/\Delta H}{(H_R - H_0)^2 + (\Delta H/2)^2} + \frac{2(H_R - H_0)[1 + \beta(H_R - H_0)/\Delta H]}{(H_R - H_0)^2 + (\Delta H/2)^2}\right] \tag{4.2}$$

Fig.4.6 shows the typical field modulated FMR data taken for LSMO on STO (111) thin film. The data in red, black and blue solid lines show the experimental, fitted, and residual curves respectively. The resonance field (H_R) and the linewidth (ΔH) can be extracted directly from the fitted function shown in Eq.(4.2).

4.4.2 Broadband FMR

The broadband FMR measurements were performed using a coplanar waveguide (CPW) and a lock-in amplifier detection technique. Fig.4.7 shows the schematic of the CPW-FMR setup. It consists of four main parts - a microwave source, a pair of electromagnets, a CPW, and a lock-in detector. A vector network analyzer (VNA) was used as a source to apply microwave current to the CPW connected through a coaxial cable. The CPW consists of a coplanar layer of three conductors in ground-signal-ground (GSG) geometry with characteristics impedance of 50 Ω. An in-plane magnetic field is applied perpendicular to the microwave field using electromagnets. The microwave current passing through the waveguide generates a microwave field which excites uniform precession of spins in the ferromagnetic sample placed on the top of the CPW. A low-amplitude magnetic field of 0.25 mT at 211.5 Hz was used to modulate the signal before lock-in detection. The measurements were performed sweeping the applied magnetic field while keeping the applied microwave frequency constant.

The frequency sweep capability of CPW-FMR allows one to investigate the frequency-field dispersion of the FMR mode described by the Kittel equation. The frequency dispersion helps in identifying modes especially when multiple resonances are observed in the measurements. The biggest advantage of this technique is that it provides valuable information about the materials's Gilbert damping parameter unlike the cavity FMR technique. The frequency-field data fitted to the Kittel equation allows us to extract an effective magnetic field inside the magnetic materials, see fig.4.8. The linewidth versus frequency data fitted to straight line allows to estimate the Gilbert damping parameter (α) and the inhomogeneous linewidth, see the fig.2.11 of the previous chapter.

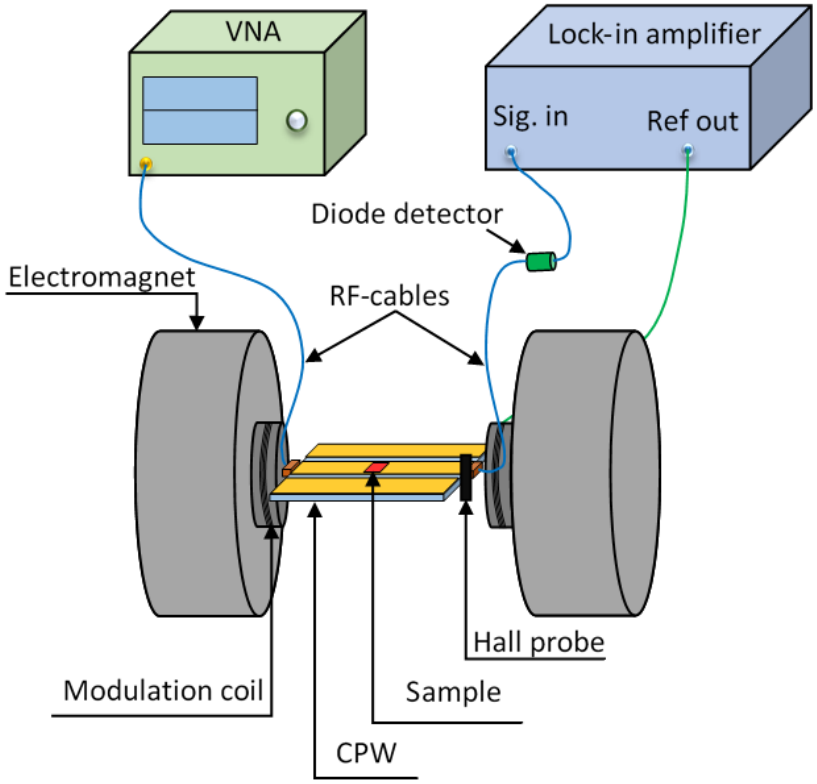

Figure 4.7: Schematic illustrating CPW-FMR setup.

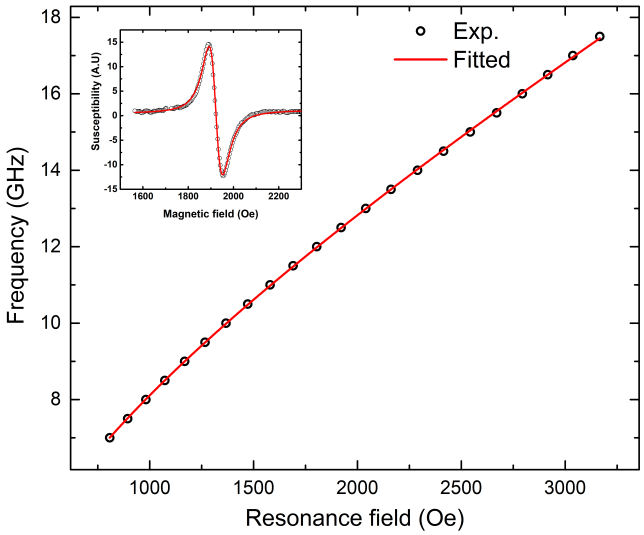

Figure 4.8: The frequency-field dispersion curve plotted for the Permalloy magnonic crystals. The black open circles and solid red lines show the experimental and the fitted data respectively. The plot in the inset shows the FMR lineshape measured for the sample FS200 of the MCs.

Chapter 5

Propagating spin-wave spectroscopy

5.1 State of the art

A conventional approach to study the magnetodynamic properties is through ferromagnetic resonance spectroscopy. This technique excites uniform magnetization precession where all the spins precess in phase and is a very convenient tool to study the static and dynamic properties of the ferromagnets [34]. However, this technique does not excite propagating spin-wave and thus lacks investigating the propagation properties of spin-waves.

For a detailed investigation of spin-wave dynamics in ferromagnets, one needs an experimental setup capable of exciting nonzero wavevector $(k\#0)$ spin waves to study their propagation characteristics. The spin-wave offers a tool to probe various magnetic interactions in addition to its potential applications in information and data processing. Recent scientific advances have demonstrated that spin waves can be used to probe spin-polarized transport and also to quantify Dzyaloshinskii-Moriya interaction (DMI) in ferromagnets [110–114]. When it comes to spin-wave application in the magnonics devices, the spin-wave characteristics parameters such as group velocity (v_g), attenuation length (Λ), and relaxation time (τ) are the important parameters controlling device functionalities. These parameters would play an important role in improving the performance of spin wave-based magnonics devices. There are very few techniques that make it possible to characterize all these parameters in a self-contained manner, we rely on propagating spin-wave spectroscopy (PSWS) which is a robust and a versatile technique capable of exciting wavelength-selective spin waves in frequency [54]

and time-domain [55]. The PSWS technique has been used widely in the scientific community to study propagation characteristics of dipolar spin waves in various magnetic thin films [54, 115–117]. It is similar to the CPW based FMR technique where the microwave current passing through the CPW excites uniform magnetization precession in the ferromagnet. However, in the PSWS technique, the microwave antennas connected to CPWs are lithographically patterned on the ferromagnet itself which excite non-uniform magnetization precession. The antenna geometry allows spin wavevector selectivity and its monochromaticity [54, 113].

The lithographically patterned microwave antenna suffers from poor efficiency due to ohmic losses and impedance mismatch which limits this technique to the excitation of long wavelength dipolar spin waves. The exchange-dominated spin waves possess a nanometer-scale wavelength, travel much faster compared to dipolar spin waves, thus are demanding for high-speed computing applications [118, 119]. Lately, this technique has been employed to excite exchange and dipole-exchange spin waves in YIG/Co(or Ni), and YIG/Co(or Ni)-MCs bilayers where the exchange and magneto dipolar coupling from the MCs layer efficiently excite nanometer scale dipole-exchange spin waves. However, the frequency of FMR mode in cobalt layer must coincide with perpendicular standing spin waves (PSSWs) frequency in the YIG layer in such bilayers [119–121].

The aim of this chapter is to discuss in detail the operating principle of PSWS, and step-wise lithography processes involved in device fabrication. Then the role of the antenna geometry on spin-wave excitation, spin wavevector selection, and impedance mismatch will be discussed in the context of the theoretical model and CST microwave simulations. At last, the PSWS experimental set-up and method of signal processing will be discussed.

5.2 Operating Principle

Propagating spin-wave spectroscopy works on the principle of electromagnetic induction. Fig.5.1 shows the schematic illustrating the excitation and detection of spin-wave. The microwave current injected in one antenna generates an Oersted field around the magnetic strip underneath the antenna which excites spin-wave in the magnetic strip. The Oersted field generated here follows the same spatial variation as the meander of the antenna and hence the spin-waves excited are forced to have the same wavelength as the wavelength of the antenna. The spin-wave excited travels in both forward and backward direction in the strip. The spin-wave propagating in the strip generates an additional magnetic flux which according to Faraday's law induce an oscillating voltage in nearby antenna. The induced voltage can be detected by the self and mutual inductance of the exciting and detecting antennas [122].

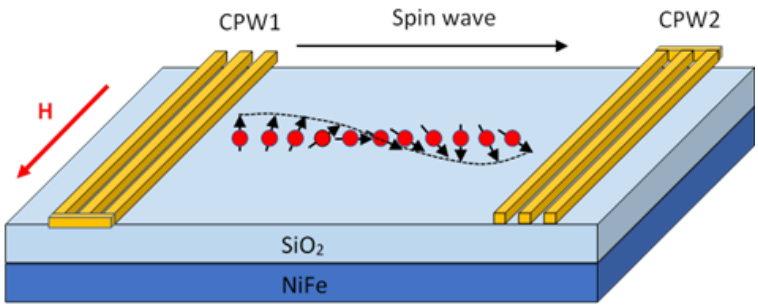

Figure 5.1: Schematic illustrating excitation of spin-wave by antenna (CPW1) and detection by antenna (CPW2). The red and black arrows show the direction of applied field and the direction of spin-wave propagation respectively.

Fig.5.2 shows the fabricated spin-wave device. The device consists of two identical gold antennas deposited on the top of a ferromagnetic (FM) strip, one for exciting spin waves and other for detection. An insulating layer is deposited in between the FM and gold layers to avoid the short circuit. The antennas are configured in the form of CPW and tapered towards the short end to avoid the formation of standing waves in the system. An alternative device with additional DC probes was also fabricated to study the impact of spin current on spin waves. The detailed process steps for the device fabrication will be discussed later in this section.

5.3 Spin-wave device fabrication

In this section, we will discuss the process steps for device fabrication. The device consists of a stack of layers Si/SiO_2/NiFe/SiO_2/Ti/Au deposited on top of each other by a combination of electron beam lithography (EBL) and lift-off techniques.

A general overview of the sample fabrication is shown in Fig.5.3. The whole process is divided into three steps. An optional four-step process is also optimized for a device with a small antenna period in order to study the effect of current-induced spin transfer torque on spin waves. In the first step, a magnetic strip was defined by ion beam etching/magnetron sputtering followed by deposition of an insulating (SiO_2) layer using electron beam evaporation in the second step. In the final step, a pair of microwave antennas connected to CPWs were deposited. The same fabrication steps were followed for the device fabrication on Co_2FeAl (CFA) thin films. The CFA thin films were deposited by ion beam sputtering. In the following section, the process involved in each process step will be discussed in detail.

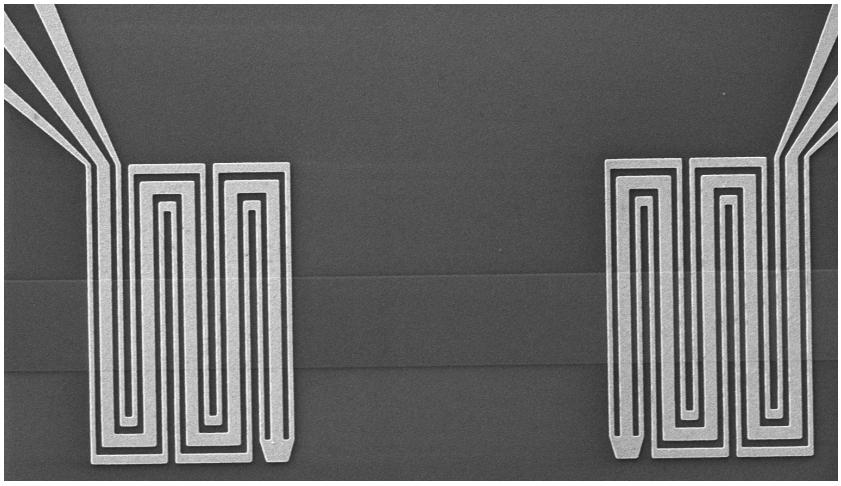

Figure 5.2: Scanning electron microscope image of the patterned microwave antennas. A strip underneath the antenna shows the ferromagnetic layer.

All the process steps for the spin wave device fabrication has been done in cleanroom facility at NTNU Nanolab.

5.3.1 Magnetic Strip

In the first step, magnetic strips of dimension 100x300 μm^2 were defined by electron beam lithography and etching/lift-off techniques on the silicon substrate. Prior to the deposition, the substrate was cleaned in acetone and isopropyl alcohol (IPA) 2 minutes each and then cleaned in oxygen plasma to remove chemical residues. After cleaning, 200 nm SiO_2 was deposited by electron beam evaporation to insulate the spin-wave device from the substrate. The sample was then spin-coated with 450 nm CSAR 62 electron beam resist, soft-baked at 230 °C for 3 minutes and finally exposed with an electron beam with a dose of 300 $\mu C/cm^2$. Subsequently, the sample was developed in developer (AR 600-546) for 1 minute and in IPA:MIBK (3:1) for 5 sec. After development the sample was cleaned in O_2 plasma for 30 sec to remove the remaining resist residues. Finally, deposition/etching of Permalloy by magnetron sputtering/ion beam etching. At end we left with a magnetic strip on Si/SiO_2 substrate, see Fig.5.3(a).

5.3.2 Insulation layer

In this step, an insulation layer was deposited to avoid shunting the magnetic strip with the microwave antennas. This step also involves resist coating, electron beam exposure, development and finally deposition of 70 nm SiO_2 by RF magnetron

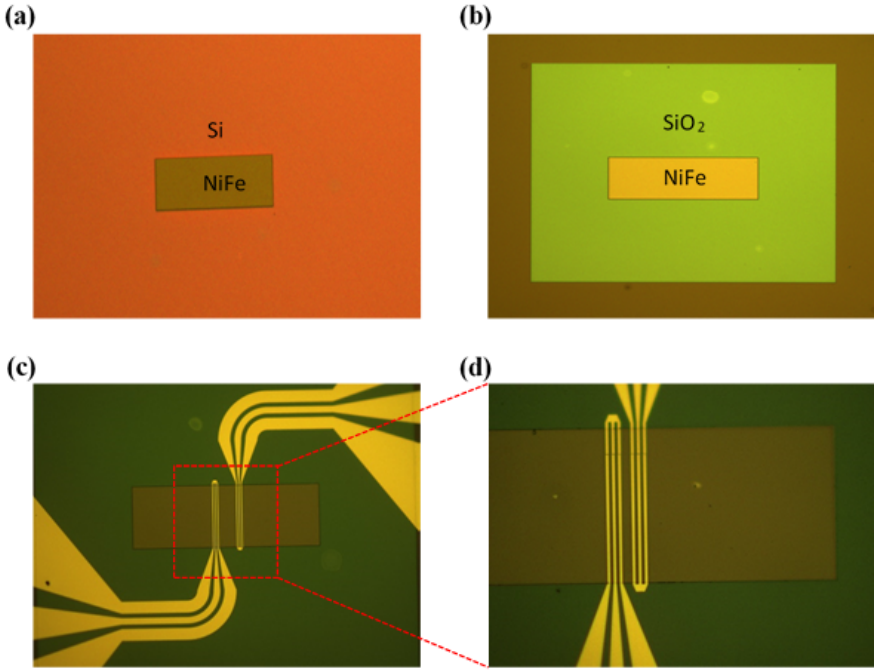

Figure 5.3: Optical microscope images of the spin-wave device taken at the various stage during the fabrication.The Fig (a), (b), and (c) show the layer structure of the device after the completion of step first, second and third respectively. The inset shows the enlarged view of microwave antennas in (d).

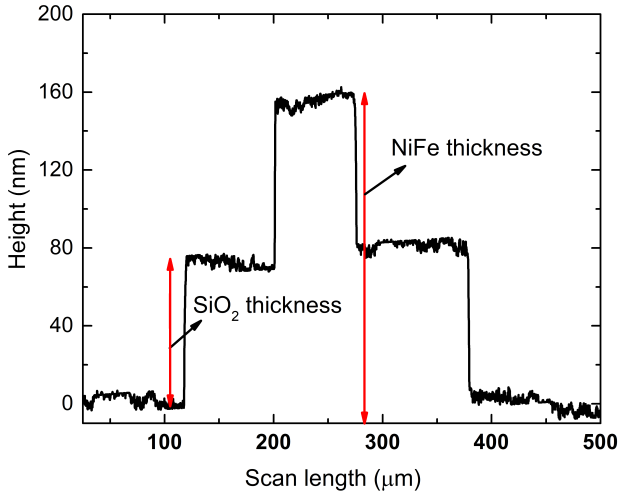

Figure 5.4: The thickness profiles of the deposited NiFe and SiO_2 layers measured by profillometer.The red arrows show the thickness of the films in nanometer.

sputtering, see Fig.5.3(b).

The thickness profile of these two deposited layers was mapped by a profillometer. Fig.5.4 shows the thickness of the NiFe and SiO_2 layers.

5.3.3 Coplanar waveguides and antennas

In this step, a pair of microwave antennas were deposited. The process step also involves the same steps of resist coating, development and layer deposition of Ti(10 nm)/Au (200 nm) by electron beam evaporation. The final fabricated spin wave device is shown in the Fig.5.3(c).

The final layer consists of large as well as small features size. So, the exposure time or the developing time after exposure might be different for large and small patterns. In order to save the resource and reduce the fabrication time, this layer was optimized for a single layer exposure instead of two using proximity effect correction described in the previous chapter.

5.3.4 Alternative approach for device fabrication

An alternative four-step process was also optimized for making a device with a very small antenna period (550 nm) in order to study the effect of current-induced

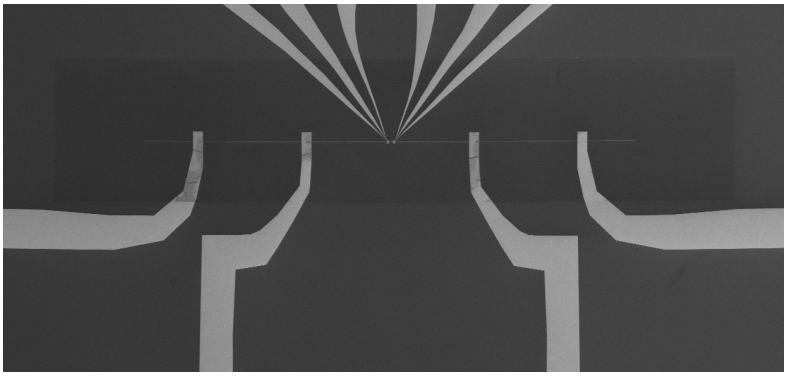

Figure 5.5: Scanning electron microscopy image of the spin wave device depicting the four DC pad and a pair of microwave antennas

spin tranfer torque on the spin waves. However, we could not perform these investigations due to the limited project time. Fig.5.5 show the SEM image of the fabricated device. Fig.5.2 shows the zoomed part of the meander shape microwave antennas. The electron beam lithography and liftoff techniques were used as described before. However, a slightly different sequence was adopted. In the first step, a magnetic strips were defined which followed by DC pads and CPWs deposition in the second step. In the third step, an insulation layer was deposited. Finally, microwave antennas with strips connecting antennas to CPWs were deposited in the fourth step.

5.4 Antenna geometry and impedance matching

As we have mentioned in the previous section, the periodicity of the antenna determines the wave vector of the excited spin waves, so varying the geometry of the pattern one can excite spin waves of the desired wavevector. The Fourier transform of the spatial distribution of current in the antenna represents the emission spectrum of excited spin waves [122]. Fig.5.6 shows the emission spectra of the antennas with the ground, signal widths and ground-signal gap of 6, 3, and $3\mu m$ respectively. The main peak which corresponds to the primary period is observed along with two weak secondary peaks.

The spin-wave was measured recording the induced voltage in the detecting antenna. A small impedance mismatch among the components such as coaxial cables, fabricated CPWs, and exciting/detecting source may cause reflection in the input signal and thus loss in input signal. Therefore, it is important to remove any possible source of reflection. The CPWs were chosen ground-signal-ground

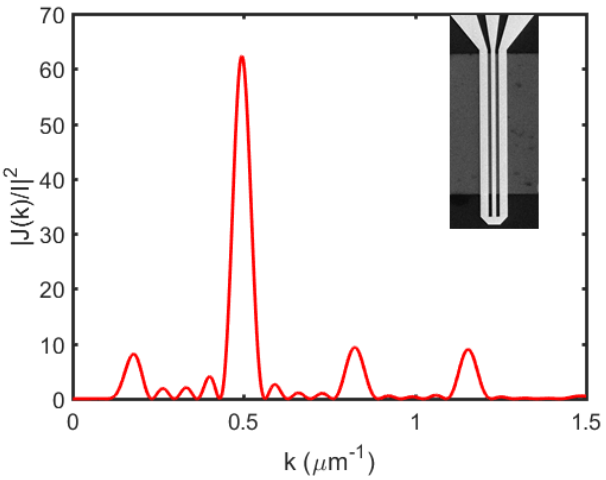

Figure 5.6: The FFT of the current density plotted as a function of wave vector for the antenna geometry shown in the inset. The main peak shows the wave vector of the spin wave to be experimentally excited by the corresponding antenna.

(GSG) configuration. All the components used in the experiment has characteristics impedance of 50 Ω, so accordingly the dimensions of the ground and signal lines and the signal-ground gap chosen to set the characteristics impedance at 50 Ω. In addition, the tapers connecting the CPWs have been chosen such as to get minimum reflections or the signal loss.

For a transmission line such as CPW, the characteristics impedance is given by [123]:

$$Z_C = \frac{1}{(\epsilon_0 c\sqrt{(8(\epsilon_r+1))}} \frac{K(\sqrt{(1-u^2)})}{K(u)} \tag{5.1}$$

where, ϵ_0 is the vacuum permittivity, ϵ_r the relative permittivity of the substrate, c the speed of light, and $K(u)$ the complete elliptic integral of the first kind with $u = a/b$. Note, this equation is only valid under the assumption that the ground planes are extended indefinitely on the either sides of the CPWs. For CPWs with finite-width ground lines, $w_g = c - b$, the factor u can be corrected to $u = \frac{a}{b}\frac{\sqrt{(c^2-b^2)}}{\sqrt{(c^2-a^2)}}$ [124], where a, b, and c are the length shown in the Fig.5.7.

5.5 CST microwave simulations

As we have mentioned in the previous section that the impedance matching is important in the microwave circuit for the maximum power delivery with minimum

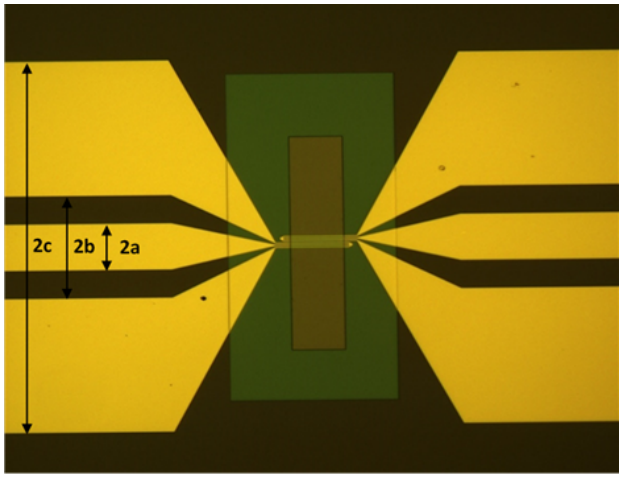

Figure 5.7: Optical microscope image of the spin wave device depicting parameters a, b, and c of the CPWs. The brown, green and the yellow color show the layers of NiFe, SiO_2, and the CPWs respectively.

loss. The impedance mismatch causes reflections in the circuit and thus a loss in the input signal. Especially, in microwave antennas where dimensions are in the sub-micrometer range, the losses due to reflections are very high. The signal loss is a major concern in the antenna based spin-wave excitation and puts a lower limit on the dimensions of the antennas and thus limitation on the wavelength of the spin wave that can be excited. Also, since the antennas are connected to CPWs through taper sections, it is important to make sure the impedance is matched well in all the sections.

We have used CST microwave simulations to make sure that the impedance of the antenna is close to characteristics impedance of 50 Ω. Fig.5.8 shows a typical model used in the simulations. Tetrahedral mess cells with adoptive mess refinement were used. A Gaussian wave was used as an excitation source and fed through the waveguide port defined at both the end of CPWs. The frequency domain solver was used in the simulations.

5.6 Experiment setup

The schematic of the homemade PSWS set-up is shown in Fig.5.9. A pair of electromagnets were used for applying the magnetic field. A picosecond voltage pulses/continuous microwave current were used as a source to excite spin waves and sampling oscilloscope/spectrum analyzer as a detector to detect the spin waves

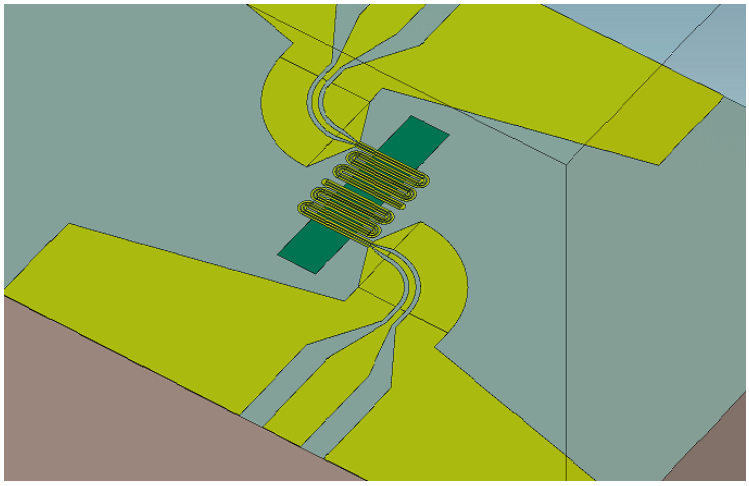

Figure 5.8: Diagram illustrating the typical model used in CST microwave simulations. The green and the yellowish parts in the model shows the Permalloy strip and the gold antennas respectively.

in the time-domain/frequency-domain. The microprobes from GGB industries were mounted on micropositioners to connect the probes to the CPWs fabricated on the sample with the help of a digital camera. Flexible coaxial cables were used to connect the probes to the source and the detector.

Time-resolved measurements were performed sending picosecond voltage pulses and the induced voltage was measured at constant magnetic field. The signal measured at zero magnetic field was taken as reference and measurement performed at the various field was subtracted from it to extract the pure spin-wave signal. The continuous spin-wave measurements were performed recording the transmitted signal at a constant microwave frequency while sweeping the applied field.

5.7 Signal processing

The spin-wave signal was measured recording the change in antenna impedance (Z_{ij}). The transmission measurements performed at various magnetic field $Z_{ij}(\omega, H)$ are subtracted from the zero-field (reference) measurements $Z_{ij}(\omega, H_{ref})$. Since the coupling between the antenna and the magnetic strip is purely inductive, the change in antenna impedance can be related to the inductance of the antenna by the relation [122]:

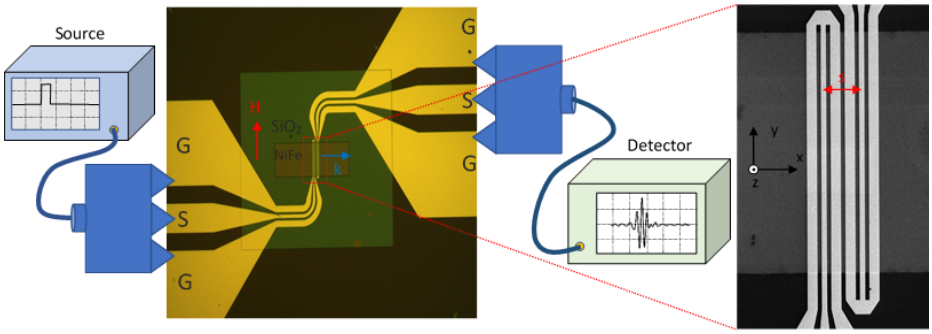

Figure 5.9: Schematic illustrating propagating spin wave spectroscopy. The optical microscope image at the center depicts the various layers of the spin-wave device - CPWs in yellow, SiO_2 in green, and Permalloy strip in brown colors. The inset shows the SEM image of the microwave antennas depicting the ground, signal and the ground-signal width of the antennas and the Cartesian coordinates.

$$\Delta L_{ij} = \frac{1}{i\omega}[Z_{ij}(\omega, H) - Z_{ij}(\omega, H_{ref})] \tag{5.2}$$

where, (i,j) = (1, 2) show the port 1 and 2 of the spin-wave device, ω is the angular frequency of the spin-wave.

The voltage induced by the spin-wave is very weak and as we know the sensitivity of the oscilloscope is not as good as the spectrum analyzer, therefore a proper signal amplification is needed to detect the spin-wave in the time domain. We have used a 20-dB low noise broadband amplifier for signal amplification. Further, to enhance the signal to noise ratio the data was averaged over 10,000 measurements. However, continuous spin-wave measurements were performed detecting the induced voltage while sweeping the magnetic field without any signal amplification.

Chapter 6

Summary and outlook

6.1 Summary

In this thesis, the magnetodynamic properties of different magnetic systems namely complex oxide—LSMO/STO (111)—heterostructure interface, NiFe, Co_2FeAl thin films and NiFe magnonic lattices has been investigated by a combination of Ferromagnetic Resonance and propagating spin-wave spectroscopy techniques. The main aim of this thesis was to provide a better understanding of magnetization dynamics in these materials which I believe would prove to be useful in the future for their practical applications in spintronic and magnonic devices.

Magnetodynamic properties of complex oxide - LSMO/STO(111) heterostructure interface

In this paper, we have investigated the magnetodynamic properties of LSMO/STO (111) ultrathin films employing cavity-based FMR technique. We report an interface mode in addition to a uniform mode in the FMR spectra. The weak intensity of the mode suggests a layer thickness order of few unit cells. Our investigations reveal the mode's hexagonal symmetry of the magnetocrystalline anisotropy matching with the (111) surface orientation of the STO substrate. This contrasts with the bulk mode symmetry which is always reported to have uniaxial symmetry caused by magnetostriction. Moreover, the mode is found coupled to bulk mode whose coupling strength is found to decrease with increasing temperature. Our findings suggest an interface ferromagnetic layer resulting from complex structural or spin and orbital reconstructions at the LSMO/STO interface. This study also sheds light on the possible scenarios which could give rise to such layer at LSMO/STO interface. This study emphasized a better understanding of a magnetic state confined

at LSMO/STO interface which could be a future prospects of 2D spintronics and could help in improving spin-dependent transport in LSMO/STO based magnetic tunnel junctions.

Tailoring the magnetodynamic properties of dipole coupled 1D magnonic crystals by dipolar coupling

In this paper, we have investigated the impact of dipolar coupling on the magnetodynamic properties varying the lattice width and the lattice separation of the magnonic crystals. We have demonstrated how the change in resonance field of the observed FMR mode on varying the lattice separation can be used to extract the dipolar field in the system. Our findings reveal a large variation in dipolar coupling as a function of lattice separation which found sufficiently large enough to effectively tailor both the static and magnetodynamic properties. The FMR mode splitting suggests magnonic bands and bandgap formation resulting from enhanced dipolar coupling on increasing the lattice width. Our investigations also demonstrate the impact of dipolar coupling on magnetic damping. The Gilbert damping parameter was found independent of dipolar coupling while a strong dependence was found for the non-homogeneous linewidth on the dipolar coupling.

Studying propagation properties of spin-wave by propagating spine-wave spectroscopy

Investigating the propagation properties of the magnetostatic surface spin waves were the focus of paper III and IV. A homemade all electrical propagating spin-wave spectroscopy in frequency and time domain was employed to investigate the spin-wave propagation properties. The work performed in the section also involves developing and optimizing process steps for fabricating nanoscale spin-wave devices as well as setting up and automizing the propagating spin-wave spectroscopy.

In paper III, we have reported a comprehensive study to investigate propagation properties of spin-wave in permalloy utilizing two different excitation sources – a voltage pulse and a continuous microwave current in time-resolved and field-sweep broadband propagating spin-wave spectroscopy respectively. This study systematically details the spin-wave propagation parameters in permalloy and their dependence on magnetic field/frequency. The method outlined in this paper can be used as a general method to extract the spin-wave propagation parameter using a continuous microwave source. This study also discusses important differences between these two complementary techniques based on the accuracy of the propagation parameters estimated.

To explore the potential of half-metallic Heusler alloy for magnonic ap-

plications, spin-wave propagation properties have been investigated in sputtered Co_2FeAl thin films in Paper IV of this thesis. This paper explores the method developed in the paper III to investigate the spin-wave propagation properties. This study investigates the propagation parameters of spin-wave and their systematic dependence on the spin-wave frequency. Our results suggest that the sputtered Co_2FeAl thin film deposited on CMOS compatible Si substrate is a promising material for magnonic device applications.

6.2 Outlook

Magnetodynamic properties of LSMO/STO (111) heterostructure interface

The induced magnetic state at the magnetite-titanate interface displays interesting magnetic properties that open a path for 2D spintronics at the interface. Understanding fundamental physical properties at such interface is crucial for practical device applications. Such a pure 2D interface state holds a great promise for magnonic device technology. Exploring the magnetodynamic damping as well as the spin-waves propagation properties in such an interface would be interesting for the device application as well as for the fundamental physics. However, characterizing such a thin layer sandwiched between two films pose a big challenge for the existing device characterization techniques.

Tailoring the magnetodynamic properties of dipole coupled 1D magnonic crystals by dipolar coupling

In tightly coupled MCs, the fundamental mode of the individual lattice coupled via dynamic dipolar coupling which results in the formation of collective mode excitation. This collective mode provides important information about the magnonic band and gap formation in MCs. Understanding the interplay of dynamic dipolar coupling on magnetodynamic properties is important for their potential applications in the magnonic filter. Thus these possibilities which require an advanced Brillouin light scattering spectroscopy remain unexplored in our investigations.

Studying spin-wave propagation properties by propagating spin-wave spectroscopy

The parasitic coupling between the exciting and detecting antenna in propagating spin-wave spectroscopy dominates at microwave frequencies. The coupling is undesired since it overlaps with the spin-wave signal and makes the detection difficult. Therefore, it is important to understand the nature of the coupling and its dependence on control parameters in order to minimize it. This coupling is found to dependent on gap distance and magnetization of the film. The behavior of coupling with gap distance is well understood however its dependence on magnetization

in combination with gap distance as well as spin-wave frequency is complex and demands a detailed investigation.

For practical applications, active control and efficient manipulation of spin-waves are desired for magnonic applications. The crystallographic direction-dependent epitaxial strain which can effectively tune the magnetic anisotropy in LSMO provides a promising way to control and manipulate spin waves and would be proved to be useful for the realization of magnonic devices. The magnetic anisotropy is also tunable by choice of the substrate. Therefore, It would be interesting to investigate the impact of strain engineered magnetic anisotropy on spin-wave propagation properties.

Chapter 7

Papers

7.1 Paper I

Magnetodynamic properties of complex oxide - $La_{0.7}Sr_{0.3}TiO_3/SrTiO_3(111)$-heterostructure interface

S. Singh, T. Bolstad, I. Hallsteinsen, T. Tybell, and E. Wahlström.

Applied Physics Letters **114** 222403 (2019)

Applied Physics Letters

Magneto-dynamic properties of complex oxide—$La_{0.7}Sr_{0.3}MnO_3/SrTiO_3$—heterostructure interface

Cite as: Appl. Phys. Lett. **114**, 222403 (2019); https://doi.org/10.1063/1.5093324
Submitted: 19 February 2019 . Accepted: 18 May 2019 . Published Online: 04 June 2019

Suraj Singh, Torstein Bolstad, Ingrid Hallsteinsen, Thomas Tybell, and Erik Wahlström

Applied Physics Letters ARTICLE scitation.org/journal/apl

Magneto-dynamic properties of complex oxide–$La_{0.7}Sr_{0.3}MnO_3/SrTiO_3$–heterostructure interface

Cite as: Appl. Phys. Lett. **114**, 222403 (2019); doi: 10.1063/1.5093324
Submitted: 19 February 2019 · Accepted: 18 May 2019 ·
Published Online: 4 June 2019

Suraj Singh,[1] Torstein Bolstad,[2] Ingrid Hallsteinsen,[2,3] Thomas Tybell,[2,4] and Erik Wahlström[1,a)]

AFFILIATIONS

[1]Center for Quantum Spintronics, Department of Physics, NTNU-Norwegian University of Science and Technology, NO-7491 Trondheim, Norway
[2]Department of Electronic Systems, NTNU-Norwegian University of Science and Technology, NO-7491 Trondheim, Norway
[3]Advanced Light Source, Lawrence Berkeley National Laboratory, Berkeley, California 94720, USA
[4]Department of Materials Science and Engineering, University of Wisconsin-Madison, Madison, Wisconsin 53706, USA

[a)]erik.wahlstrom@ntnu.no

ABSTRACT

We have studied the interface magnetodynamic properties of $La_{0.7}Sr_{0.3}MnO_3/SrTiO_3$ (111) heterostructures by Ferromagnetic resonance spectroscopy (FMR). In addition to the bulk FMR mode, the measurements indicate a mode originating from an independently excited ferromagnetic layer at the interface. The peak-to-peak intensity of the interface mode suggests a layer thickness on the order of few unit cells. Angle resolved FMR measurements reveal a hexagonal symmetry of the magnetocrystalline anisotropy of the mode with the easy axis along the in-plane <1–10> crystallographic directions matching with the (111) surface orientation of the substrate, in contrast to bulk mode symmetry which is always found to have uniaxial symmetry caused by magnetostriction. The temperature dependence of the anisotropy and a large temperature variation in the intensity ratio of interface and bulk mode indicate a coupling of the interface to the bulk mode.

Manganite-titanate interfaces have attracted a lot of attention for their novel physical properties driven by structural, electronic, and orbital reconstructions. A variety of interesting phenomena such as induced ferromagnetism, superconductivity, metal-insulator transition, and multiferroics have been observed at such interfaces.[1,2] The interface induced ferromagnetism in such systems is of fundamental interest, while at the same time, the presence of the magnetic states confined to the interface opens new perspectives for 2D spintronics at oxide interfaces and may have an impact on spin dependent transport properties of novel spintronics devices such as magnetic tunnel junctions (TMJs).[3,4] In several (001) oriented manganite/titanate interfaces such as $LaMnO_3/SrTiO_3$,[5] $La_{0.7}Sr_{0.3}MnO_3/SrTiO_3$,[6] (LSMO/STO) and $La_{0.7}Sr_{0.3}MnO_3/BaTiO_3$,[7] Ti-induced interface ferromagnetism has been observed and is ascribed to orbital and spin reconstructions. An enhanced interlayer coupling has been reported in the $La_{0.7}Sr_{0.3}MnO_3/SrTiO_3$ (001) heterostructure due to the induced ferromagnetism which could improve the performance of $La_{0.7}Sr_{0.3}MnO_3/SrTiO_3$ TMJs.[5] The (111) oriented interfaces of such a heterostructure are more prone to interface-induced emergent phenomena due to a terminating polar layer, where surface Ti atoms form a honeycomb lattice that hosts orbitals with hexagonal symmetry.[2,8] However, detailed investigations of interface ferromagnetism in $La_{0.7}Sr_{0.3}MnO_3/SrTiO_3$ (111) interfaces are still missing. Investigation of such interfaces can thus give important information in order to develop a coherent understanding of the underlying physics and further their successful implementation in device applications.

The atomic layers close to the manganite-titanate interface are central for understanding this emergent phenomenon and to elucidate their potential for spintronics applications. Studies of such buried interfacial layers using nondestructive techniques are advantageous over techniques that involve sample cleavage. Ferromagnetic Resonance (FMR) spectroscopy is in this regard an interesting technique, exhibiting large sensitivity that should enable studies of magnetic interface properties of complex oxide heterostructures. To be observable as a separate interface mode, the magnetic interface layer should preferably be weakly coupled to the bulk ferromagnetic layer and display different magnetic properties from the bulk.[9] In manganites, the ferromagnetic ordering is often suppressed at the interface due to changes in the Mn^{3+}/Mn^{4+} ratio, where Mn^{3+} enriched layers have a decreased double exchange coupling.[10,11] Hence, in such a system, exciting and detecting interface modes should be easier as compared to metallic ferromagnets where spins are tightly exchange coupled at an interface.

In this letter, we report the magnetodynamic properties of the LSMO/STO (111) heterostructure using angle resolved FMR spectroscopy. We show that an interface mode in FMR spectra arises, connected to an interface ferromagnetic layer, from structural or electronic and orbital reconstructions. Furthermore, we show how this mode can be used to extract some important properties of the LSMO/STO interface. The intensity observed indicates a sensitivity that well matches the expected signal from an interface layer thickness on the order of few unit cells. Moreover, the observed hexagonal symmetry of the mode shows that the magnetocrystalline anisotropy is dominant over the magnetostriction in contrast to the bulk mode that always found dominated uniaxial anisotropy caused by magnetostriction.

Epitaxial LSMO thin films were grown on (111)-oriented STO substrates by pulsed laser deposition from stoichiometric targets. Prior to deposition, the substrates were cleaned in de-ionized water at 70 °C in an ultrasonic bath and then annealed for 1 h at 1050 °C in an oxygen environment. The growth took place with an oxygen background pressure of 0.35 mbar and a substrate temperature of 540 °C. The substrate to target separation was kept fixed at 45 mm. A KrF excimer laser ($\lambda = 248$ nm) with a fluency of 2 J cm^{-2} and a repetition rate of 1 Hz was used to ablate the material from the target. After the deposition, the samples were cooled to room temperature at the rate of 15 K/min. The surface morphology was characterized by atomic force microscopy (AFM, Veeco Nanoscope V). The imaged step and terrace structure are consistent with films deposited on the vicinal substrate. More information on growth can be found elsewhere.[12,13] The magnetic moment measurements were performed using a Vibrating sample magnetometer (VSM). The in-plane magnetization hysteresis (M-H) loops measured at 50 K are shown in Fig. S5 of the supplementary material. The thermomagnetization measurements (M-T) can be found elsewhere.[14] The magnetodynamic properties were studied by X-band Electron Paramagnetic Resonance (EPR/FMR) with a fixed microwave frequency of 9.4 GHz (Bruker Bio-spin ELEXSYS 500, with a cylindrical TE-011 microwave cavity). The sample is attached to a quartz rod and mounted along the symmetry (z-axis) in the cylindrical cavity. The rod is attached to a goniometer allowing us to rotate the sample 360° in-plane and out of plane. A microwave field is applied perpendicular to the sample plane in the cavity. The applied static magnetic field is then swept to record the FMR absorption. The FMR absorption is taken for 10, 15, and 30 nm LSMO thin films at various in-plane angles (φ), an angle between the applied magnetic field and the [1-10] crystallographic direction of the film, at a precision of 2° shown in Fig. 1(a). The measurements were taken at room temperature as well as low temperature using a liquid nitrogen cryostat.

The angle (φ) dependent in-plane FMR spectra acquired show that in contrast to a single FMR mode expected for ultrathin epitaxial films, all our samples display at least two similar modes labeled as I_M and FMR,[15] indicated by black arrows in Figs. 1(b) and S1 of the supplementary material. We focus on the mode I_M which is consistently found in all the investigated films and is a candidate for an interface mode. This mode displays a different symmetry from the uniform mode. To investigate the possible origin of this mode, we have plotted the f (H) dispersion curve for various possible spin waves (see the supplementary material) for an in-plane magnetized 15 nm LSMO thin film at room temperature in Fig. 2(b). The intersection of the spin wave dispersions with the measurement frequency (9.4 GHz) of the cavity FMR spectroscopy, shown as a horizontal line, is related to the

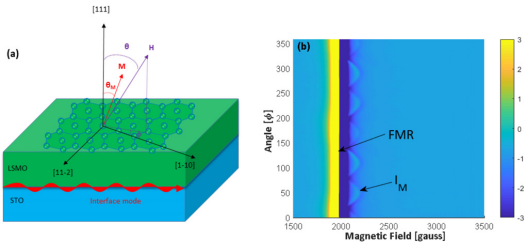

FIG. 1. (a) The schematic of the LSMO/STO heterostructure having hexagonal in-plane symmetry. Azimuthal angle (ϕ) dependent X-band 2D-FMR spectra of LSMO 15 nm at RT in (b). Black arrows in the figure indicate the detected modes.

possible resonance field of the corresponding modes. As shown in Fig. 2(a), the resonance field of mode I_M is always found at higher fields than the FMR mode. Such a high field mode observed in in-plane FMR measurements can be ascribed to an exchange dominated surface mode due to surface spin pinning.[16–18] However, the mode is not found to follow the characteristics of surface modes (see the supplementary material),[18–20] and hence, a surface mode can be discarded. The frequency of the perpendicular standing spin wave (PSSW), the first mode of the spin wave resonances, is found too far away from the measurement frequency to be detected in our measurement geometry. The magnetostatic surface (MSSW) and the backward volume magnetostatic spin wave (BVMSW) excitation require a highly localized microwave field across the sample, which is in contrast to the uniform field in our cavity measurements.[21] Also, the resonance fields expected for these MSSW and BVMSW modes do not match with the resonance field for the observed I_M. Hence, they are also unlikely. Another more probable possibility is a layer that has an effective magnetization lower than the bulk. As can be seen, the dispersion curve for such a mode having effective magnetization ($H_{eff} = 2500$ Oe) approximately $32 \pm 5\%$ smaller than the bulk plotted by the solid pink line matches well with the observed resonance field. Hence, we refer the mode I_M as a mode emerging from the interface having a lower magnetization than the bulk of the thin film. This is in accordance with Bing *et al.*, who have previously reported such a high resonance field mode as an interface mode.[9] However, impure inclusions in the film with different magnetic properties may also cause such a mode in FMR spectra. In order to exclude this possibility, out-of-plane FMR spectra, as shown in Fig. 2(c), were analyzed. The mode I_M is found to follow the behavior of the bulk mode, which indicates that it emerges from a thin planar geometry and not from impurities. Thus, the high resonance field appearance in all samples probed and the lower energy of the mode, compared to the bulk mode, clearly point toward I_M being an interface mode in contrast to exchange dominated surface modes which would have a much higher energy in such ultrathin films.

Furthermore, the ferromagnetic linewidth of the interface mode and peak to peak intensities were analyzed. The weak mode intensity prevents intensity and linewidth extraction from curve fitting. However, the mode is significant, and the trends are real and observable, and so the peak-to-peak intensity and linewidths were measured. The linewidths are always found larger than that of the bulk mode as expected for the interface mode see Fig. S4 in the supplementary material. The peak-to-peak intensity investigated from the FMR line

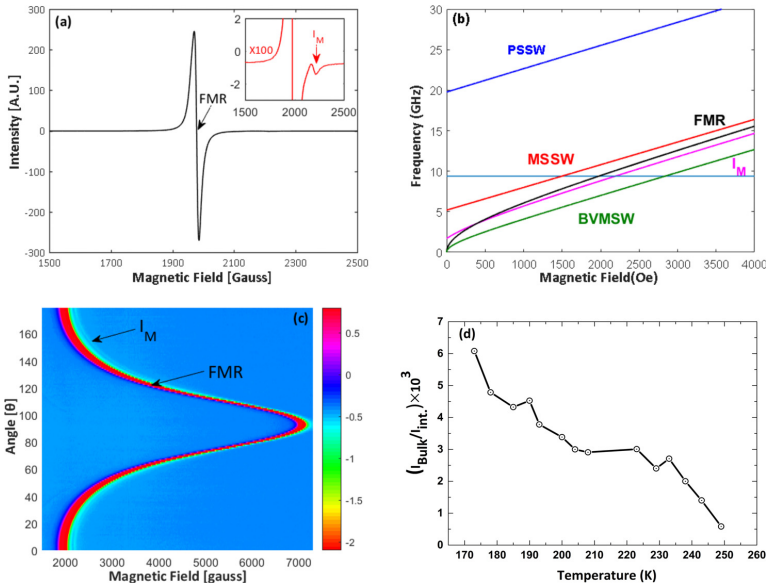

FIG. 2. (a) The FMR absorption spectra taken at a fixed in-plane magnetic field from the 15 nm film. The figure in the inset shows the zoomed y scale of (a). The interface mode is indicated by the red arrow. (b) The f (H) dispersion curve plotted for the perpendicular standing spin wave (PSSW), magnetostatic surface spin wave (MSSW), backward volume surface spin wave, uniform mode (FMR), and interface mode (I_M) and are shown by solid blue, red, green, black, and pink lines, respectively. The pink curve shows the dispersion curve for an interface mode having effective magnetization lower than the bulk mode. The cyan horizontal line shows the measurement frequency (9.4 GHz) of cavity FMR spectroscopy. (c) The polar angle (ϑ) dependent 2D-FMR spectra of the 15 nm film taken at RT. (d) The intensity ratio of the bulk and interface mode shown against temperature. The decrease in the intensity ratio with increasing temperature indicates a decrease in coupling of the interface mode to the bulk.

shape is shown in Fig. 2(d). The FMR signal intensity depends on layer magnetization, the film thickness, and applied microwave power, fixed throughout the measurements.[22,23] A quantitative analysis of the interface mode's intensity points to an interfacial layer on the order of few unit cells, in agreement with the reported values for interface magnetism in the LSMO/STO system and is consistent with the mode originating from a very thin interfacial layer.[6] We note that the intensity ratio between the bulk and interface mode is on the order of 10^3 for all investigated films, varying with temperature as shown in Fig. 2(d). The large temperature variation in the intensity ratio indicates that the interface mode is coupled to the bulk mode, albeit the coupling strength decreases with increasing temperature.[23,24]

To further investigate the temperature dependence and coupling of the two modes, we look at angle dependent measurements. It is evident from the angle dependent measurements [Fig. 1(b)] that I_M display a hexagonal symmetry which matches the LSMO/STO's (111) in-plane symmetry with easy axes along ⟨1–10⟩ crystallographic directions. Thus, the magnetic anisotropy of the interface layer is firmly related to the underlying crystal structure and is consistent with hexagonal magnetocrystalline anisotropy microscopically reported in LSMO/STO (111).[25–27] However, the value of such a huge anisotropy field observed is still not clear, and interface induced complex processes may be responsible for this. In contrast to the interface mode, the FMR mode is observed with uniaxial symmetry, see Fig. S3 in the supplementary material, which is also found to be consistent with reported step edge induced uniaxial anisotropy.[28–30] Temperature dependent FMR measurements were acquired at a fixed in-plane orientation as depicted in Figs. 3(a) and 3(b) to explore this difference. A different temperature response is observed for I_M and the bulk mode. The angle resolved FMR measurements were repeated as a function of temperatures, see Fig. S2 of the supplementary material, and the effective magnetic anisotropy field, H_6, extracted from the difference between maximum and minimum resonance fields for the interface mode is shown in Fig. 3(c). The FMR mode's anisotropy field, H_U, however, is extracted from the fitting, see Fig. S3(a) and S3(b) and shown in Fig. 3(d). The magnetic anisotropy field of both modes is found to increase with the decrease in temperature, which could be due to approaching Curie temperature (T_C). However, such a huge change in the magnetic anisotropy field for the interface mode, two orders of magnitude higher than that of the bulk mode, cannot be solely explained by changes in T_C. One possibility is that the anisotropy field of I_M is lowered due to a weaker coupling strength with increasing temperature. We also noticed an increase in mode intensity along ⟨1–10⟩ crystallographic directions in the angle dependent FMR measurement, see Fig. 1(b). This shows that the coupling strength has a directional dependence and the maximum along the easy direction.[31]

There are different possible scenarios, which could be responsible for the magnetodynamically active interface layer in such a system. For example, there is a reported a-site cation mixing of 1–2 d_{111} layers at the interface,[13] resulting in an effective (La,Sr)TiO_3 layer at the substrate side. However, such compositions are not reported to be ferromagnetic.[32] Also, if a weakening of ferromagnetism due to a changed Mn^{3+}/Mn^{4+} ratio approaching the interface would be responsible, then one would expect a stronger coupling to the bulk mode and no change in symmetry of the interface mode. Other possibilities include interface-induced ferromagnetism either due to electronic reconstruction[2] or due to oxygen vacancies at the interface.[3] Such processes result in a changed valence state of the Ti ions in STO at the interface and thereby orbital and spin reconstructions, which generates a magnetic

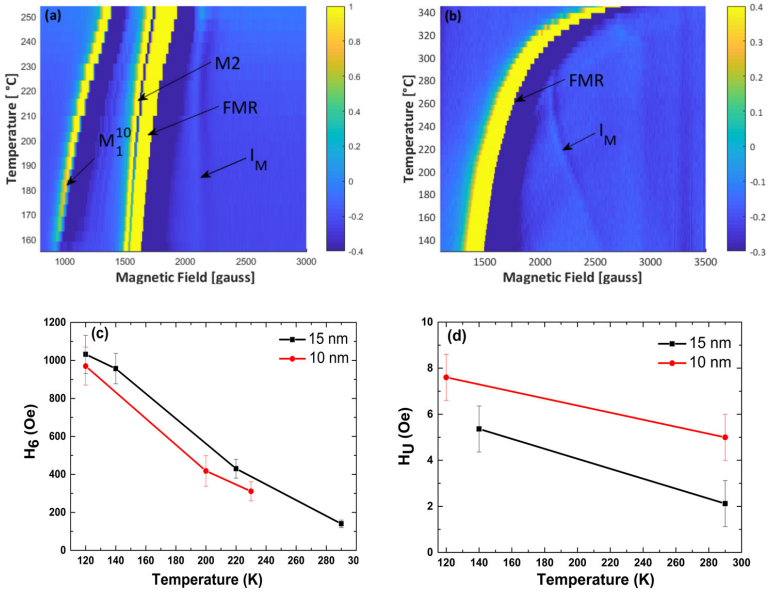

FIG. 3. Temperature dependent FMR spectra of LSMO 10 (a) and 15 nm (b) at fixed in-plane magnetic field orientation. The magnetic anisotropy fields H_6 and H_U extracted for the interface and bulk mode from the in-plane angle (ϕ) dependent FMR measurements at different temperatures for 10 and 15 nm films in (c) and (d), respectively.

state at the interface.[33] However, it has not been reported in LSMO/STO (111), and hence, further measurements are required to confirm that Ti-induced ferromagnetism is responsible for the observed interface ferromagnetism.

In summary, we have studied the magnetodynamic properties of the LSMO/STO heterostructure interface by angle resolved FMR. We found a weak low energy mode in the FMR spectra in addition to the bulk mode. Comparisons with calculations for the possible spin waves in the system indicate that the observed mode is an interface mode rather than exchange or dipole surface spin waves. The mode intensity shows that the layer thickness is on the order of few unit cells matching well with previous reports. The mode is found with hexagonal symmetry, matching with the LSMO/STO's (111) in-plane symmetry, in contrast to the bulk mode's symmetry, which is always found to have uniaxial symmetry. The anisotropy field of hexagonal symmetry is found to be highly temperature dependent. The decrease in magnetic anisotropy with increasing temperature for both modes points that the modes are coupled. Moreover, the intensity ratio of the modes, as well as the relative temperature dependence on the anisotropy field, is found to decrease with increasing temperature, which both indicate that the coupling strength is also seen to decrease with increasing temperature. These findings suggest that an interface ferromagnetic layer at the LSMO/STO interface results from structural or orbital and spin reconstructions having a hexagonal magnetocrystalline anisotropy in contrast to the bulk mode symmetry. Taken together, this study shows that it is possible to induce and detect interface magnetodynamic modes at oxide interfaces, opening a pathway for interface engineering of magnetic-dynamic systems for spintronics applications.

See the supplementary material for Kittel's quadratic relation for surface mode exclusion, the dispersion relations of the possible spin waves considered, the angle dependent FMR measurements at room temperature for 10 and 30 nm films and at low temperatures for 15 nm film, peak to peak linewidth, fitting and fitting parameters used to extract the magnetic anisotropy field, and in-plane hysteresis loops measured at 50 K.

This work was partly supported by the Research Council of Norway through its Center of Excellence funding scheme, project number 262633, "QuSpin." T.T. and T.B. acknowledge the Research Council of Norway for providing funding through Grant No. 231290. S.S. acknowledges partial funding obtained from the Norwegian Ph.D. Network on Nanotechnology for Microsystems, which is sponsored by the Research Council of Norway, Division for Science, under Contract No. 221860/F40.

REFERENCES

[1]H. Y. Hwang, Y. Iwasa, M. Kawasaki, B. Keimer, N. Nagaosa, and Y. Tokura, Nat. Mater. **11**, 103 (2012).
[2]J. Chakhalian, A. J. Millis, and J. Rondinelli, Nat. Mater. **11**, 92 (2012).
[3]Y. Suzuki, APL Mater. **3**, 062402 (2015).
[4]F. Y. Bruno, M. N. Grisolia, C. Visani, S. Valencia, M. Varela, R. Abrudan, J. Tornos, A. Rivera-Calzada, A. A. Ünal, S. J. Pennycook, Z. Sefrioui, C. Leon, J. E. Villegas, J. Santamaria, A. Barthélémy, and M. Bibes, Nat. Commun. **6**, 6306 (2015).
[5]J. Garcia-Barriocanal, J. C. Cezar, F. Y. Bruno, P. Thakur, N. B. Brookes, C. Utfeld, A. Rivera-Calzada, S. R. Giblin, J. W. Taylor, J. A. Duffy, S. B. Dugdale, T. Nakamura, K. Kodama, C. Leon, S. Okamoto, and J. Santamaria, Nat. Commun. **1**, 82 (2010).

[6]F. Y. Bruno, J. Garcia-Barriocanal, M. Varela, N. M. Nemes, P. Thakur, J. C. Cezar, N. B. Brookes, A. Rivera-Calzada, M. Garcia-Hernandez, C. Leon, S. Okamoto, S. J. Pennycook, and J. Santamaria, Phys. Rev. Lett. **106**, 147205 (2011).
[7]Y. Liu, J. Tornos, S. G. E. te Velthuis, J. W. Freeland, H. Zhou, P. Steadman, P. Bencok, C. Leon, and J. Santamaria, APL Mater. **4**, 46105 (2016).
[8]D. Doennig, W. E. Pickett, and R. Pentcheva, Phys. Rev. Lett. **111**, 126804 (2013).
[9]P. Chu-Bing and D. Dao-Sheng, J. Magn. Magn. Mater. **114**, 249 (1992).
[10]J. S. Lee, D. A. Arena, P. Yu, C. S. Nelson, R. Fan, C. J. Kinane, S. Langridge, M. D. Rossell, R. Ramesh, and C. C. Kao, Phys. Rev. Lett. **105**(25), 257204 (2010).
[11]A. Tebano, C. Aruta, S. Sanna, P. Medaglia, G. Balestrino, A. Sidorenko, R. De Renzi, G. Ghiringhelli, L. Braicovich, V. Bisogni, and N. Brookes, Phys. Rev. Lett. **100**(13), 137401 (2008).
[12]I. Hallsteinsen, J. E. Boschker, M. Nord, S. Lee, M. Rzchowski, P. E. Vullum, J. K. Grepstad, R. Holmestad, C. B. Eom, and T. Tybell, J. Appl. Phys. **113**(18), 183512 (2013).
[13]I. Hallsteinsen, M. Nord, T. Bolstad, P.-E. Vullum, J. E. Boschker, P. Longo, R. Takahashi, R. Holmestad, M. Lippmaa, and T. Tybell, Cryst. Growth Des. **16**, 2357 (2016).
[14]V. Flovik, F. Macià, S. Lendínez, J. M. Hernàndez, I. Hallsteinsen, T. Tybell, and E. Wahlström, J. Magn. Magn. Mater. **420**, 280 (2016).
[15]A. K. Pradhan, J. B. Dadson, D. Hunter, K. Zhang, S. Mohanty, E. M. Jackson, B. Lasley-Hunter, K. Lord, T. M. Williams, R. R. Rakhimov, J. Zhang, D. J. Sellmyer, K. Inaba, T. Hasegawa, S. Methews, B. Joseph, B. R. Sekhar, U. N. Roy, Y. Cui, and A. Burger, J. Appl. Phys. **100**, 033903 (2006).
[16]J. T. Yu, R. A. Turk, and P. E. Wigen, Phys. Rev. B **11**, 420 (1975).
[17]Y.-L. Zhao, Y. Sun, L.-Q. Pan, K.-S. Li, and D.-B. Yu, Appl. Phys. Lett. **102**, 042404 (2013).
[18]H. Puszkarski, Prog. Surf. Sci. **9**, 191 (1979).
[19]C. Kittel, Phys. Rev. **110**, 1295 (1958).
[20]X. Liu, Y. Zhou, and J. Furdyna, Phys. Rev. B **75**, 195220 (2007).
[21]V. Flovik, F. Maciá, A. D. Kent, and E. Wahlström, J. Appl. Phys. **117**, 143902 (2015).
[22]Y.-C. Chen, D.-S. Hung, Y.-D. Yao, S.-F. Lee, H.-P. Ji, and C. Yu, J. Appl. Phys. **101**, 09C104 (2007).
[23]A. Layadi and J. O. Artman, J. Magn. Magn. Mater. **92**, 143 (1990); **176**,175 (1997).
[24]H. Puszkarski, Phys. Status Solidi (b) **171**, 205 (1992).
[25]I. Hallsteinsen, E. Folven, F. K. Olsen, R. V. Chopdekar, M. S. Rzochowski, C. B. Eom, J. K. Grepstad, and T. Tybell, APL Mater. **3**, 062501 (2015).
[26]P. K. Rout, I. Agireen, E. Maniv, M. Goldstein, and Y. Dagan, Phys. Rev. B **95**, 241107(R) (2017).
[27]L. Miao, R. Du, Y. Yin, and Q. Li, Appl. Phys. Lett. **109**, 261604 (2016).
[28]M. Mathews, F. M. Postma, J. C. Lodder, R. Jansen, G. Rijnders, and D. H. A. Blank, Appl. Phys. Lett. **87**, 242507 (2015).
[29]P. Perna, C. Rodrigo, E. Jiménez, F. J. Teran, N. Mikuszeit, L. Méchin, J. Camarero, and R. Miranda, J. Appl. Phys. **110**, 013919 (2011).
[30]T. Bolstad, E. Lysne, U. L. Österberg, and T. Tybell, J. Magn. Magn. Mater. **487**, 165304 (2019).
[31]B. Heinrich, J. F. Cochran, M. Kowalewski, J. Kirschner, Z. Celinski, A. S. Arrott, and K. Myrtle, Phys. Rev. B **44**, 9348 (1991).
[32]J. E. Sunstrom, S. M. Kauzlarich, and P. Klavins, "Synthesis, structure and properties of $La_{1-x}Sr_xTiO_3$ ($0 \leq x \leq 1$)," Chem. Mater. **4**, 346–353 (1992).
[33]N. Pavlenko, T. Kopp, E. Y. Tsymbal, J. Mannhart, and G. A. Sawatzky, Phys. Rev. B **86**, 064431 (2012).

Supplementary information for Magneto-dynamic properties of Complex Oxide - $La_{0.7}Sr_{0.3}MnO_3/SrTiO_3$ - Heterostructure Interface

Suraj Singh[1], Torstein Bolstad[2], Ingrid Hallsteinsen[2,3], Thomas Tybell[2,4], and Erik Wahlström[1]

[1]Center for Quantum Spintronics, Department of Physics, NTNU - Norwegian University of Science and Technology, NO-7491 Trondheim, Norway

[2]Department of Electronic Systems, NTNU - Norwegian University of Science and Technology, NO-7491 Trondheim, Norway

[3]Advanced Light Source, Lawrence Berkeley National Laboratory, Berkeley, California 94720, USA

[4]Department of Materials Science and Engineering, University of Wisconsin-Madison, Madison, WI 53706, USA

Angle dependent FMR measurements at room temperature

Fig. S1 shows the angle resolved FMR measurements of 10 nm and 30 nm LSMO films at RT. In addition to FMR and I_M mode mentioned in the letter, other observed modes are labelled as mode M_1^{10}, M2, and M3 and indicated by black arrows. The mode M_1^{10}, where superscript shows the film thickness, is observed in only 10 nm and the mode M3 in 15 nm and 30 nm respectively. The modes M2, I_M and FMR mode are observed in all the investigated films.

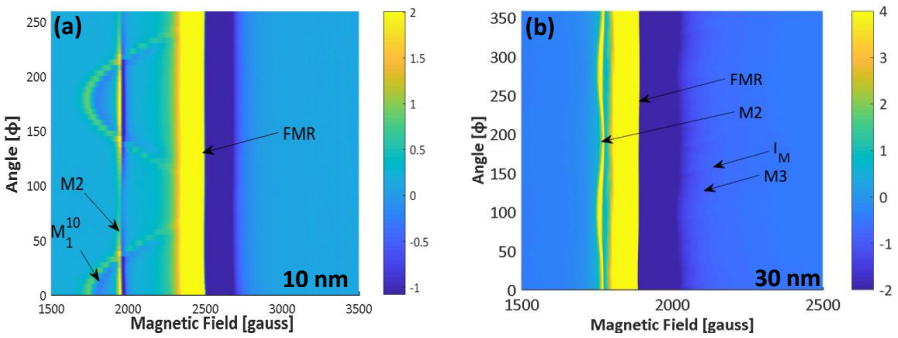

Fig. S1 Angle resolved FMR measurements at RT for 10 and 30 nm LSMO films.

Angle dependent FMR measurements at various temperatures

Angle resolve FMR measurements for different temperatures for 10 and 15 nm films are shown in the fig S2. It was found that the magneto-crystalline anisotropy field of the hexagonal symmetry decreases with increasing temperature.

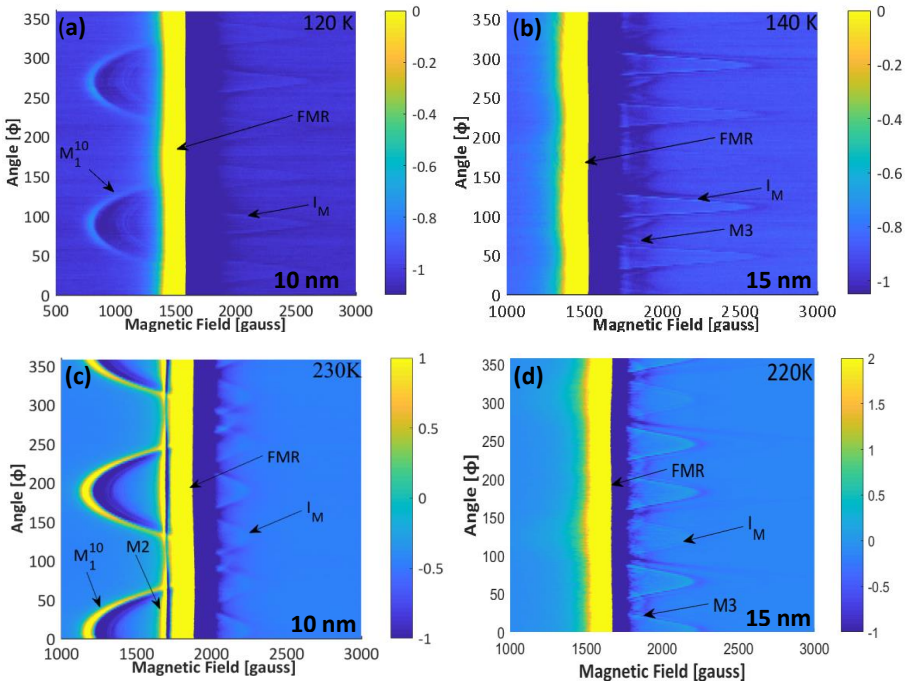

Fig. S2 Angle resolved FMR measurement of LSMO 10 nm in fig S2 (a), S2 (c) and 15 nm in fig S2 (b), S2 (d) at the temperatures mentioned at right top corner of each fig.

Extracting FMR mode's magnetic anisotropy field

The ferromagnetic resonance field of FMR mode was extracted after fitting the FMR absorption to the sum of derivative of symmetric and antisymmetric Lorentzian functions [1]. The extracted resonance fields at various in-plane angle (ϕ) were then fitted to equation (1) to extract the anisotropy field, see fig. S3(a), and S3(b).

$$f = f_0 + A\sin 2(\phi - \phi_A) + B\sin 4(\phi - \phi_B) + C\sin 6(\phi - \phi_C) \qquad (1)$$

where, f_0, *A, B and C* are fitting parameters. ϕ_A, ϕ_B and ϕ_C are the phase shifts. The values of the B, and C are found very small hence neglected. The value 2A which gives the uniaxial anisotropy field is shown in the fig. 3 (d)

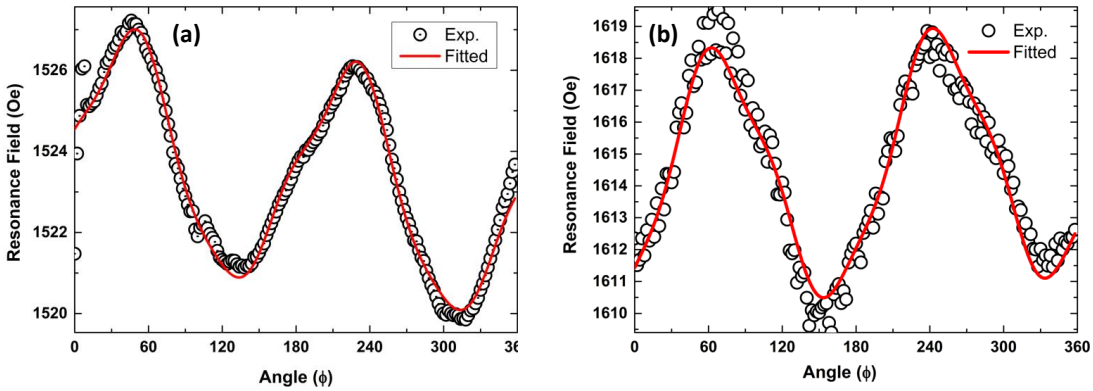

Fig. S3 Angle dependent ferromagnetic resonance field extracted after fitting the FMR line shape for 15 nm film at 140K fig S3 (a) and for 10 nm at 120K fig S3 (b). The plot shows the uniaxial anisotropy for the mode.

Peak to peak linewidth

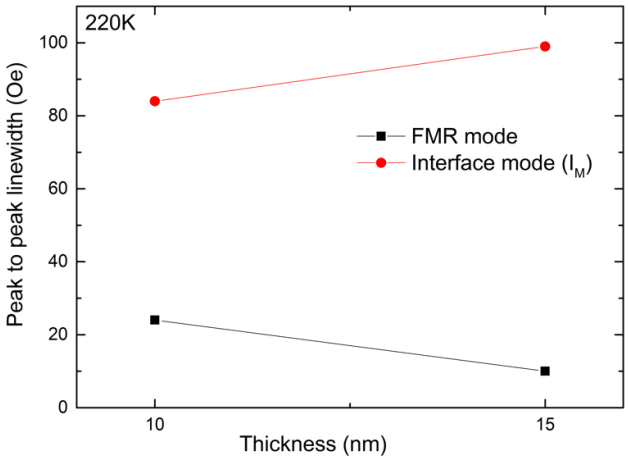

Fig. S4 The peak-to-peak linewidth measured for the FMR mode and interface mode for 10 and 15 nm films at 220K

In-plane hysteresis loops of samples at 50K

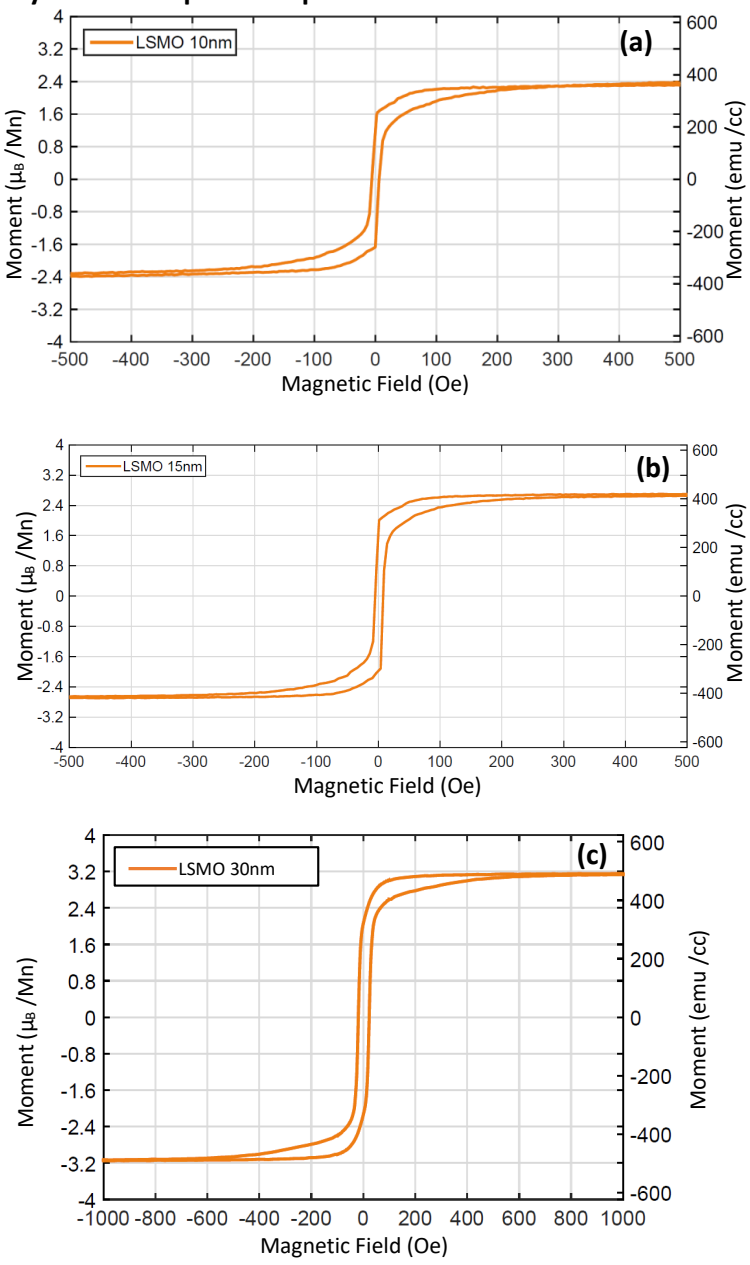

Fig. S5 The M-H loop of 10, 15 and 30 nm thin films measured by Quantum design Vibrating sample magnetometry at 50K.

Analysis of other possible spin waves:

To elucidate if the I_M data fit a surface mode we have also considered the Puszkarski's surface inhomogeneity (SI) model [2]. According to this model, surface spins are tightly pinned due to the surface anisotropy which results in excitation of perpendicular spin waves (PSSW), or spin wave resonances (SWR), whose n^{th} mode is given by the Kittel relation [3]

$$H_n = H_0 - n^2 \frac{D}{g\mu_B}\frac{\pi^2}{d^2} \quad (2)$$

where, H_0 is the position of the theoretical uniform mode, D is the exchange stiffness, and its value for LSMO is 144 meV·Å^2, and $D/g\ \mu_B$ = 12.42 T·nm^2. Based on equation (2), the difference between the uniform mode and the first body mode is large, around 5440 Oe for a 15 nm thick film. We note that this range falls outside of our measurement limit, and hence cannot be observed in our set-up. Hence, as I_M is observed close to the FMR mode, the possibility of the I_M mode to be a member of SWR due to spin pinning is very low. We have also analyzed the angular dependence of the extra (I_M)mode - spin wave resonances exhibit a critical angle in in-plane and out-of-plane rotation measurements. This occurs when all modes merge into a single mode. As magnetic field's direction is tilted away from this critical angle, the first body mode transformed to surface mode and vice-versa [4,5]. The mode I_m doesn't show any such characteristics. We accordingly conclude that the mode I_M is not a spin wave resonances or a surface mode.

Spin wave dispersion relations used

The following relations have been used to plot the dispersion curves [6-8]:

$$f = \frac{\gamma}{2\pi}\sqrt{H_r(H_r + H_{eff})} \qquad \text{Kittel}$$

$$f = \frac{\gamma}{2\pi}\sqrt{(H_r + Dk^2)(H_r + H_{eff} + Dk^2)} \qquad \text{PSSW}$$

$$f = \frac{\gamma}{2\pi}\sqrt{H_r(H_r + H_{eff}) + H_{eff}^2\left(\frac{1 - e^{-2k\prime d}}{4}\right)} \qquad \text{MSSW}$$

$$f = \frac{\gamma}{2\pi}\sqrt{H_r\left(H_r + H_{eff}\left(\frac{1 - e^{-k\prime d}}{k'd}\right)\right)} \qquad \text{BVMSW}$$

Here, f is frequency of the cavity, γ is the gyromagnetic ratio, where $\gamma/2\pi \approx 28$ GHz/T, H_r is resonance field, d is the thickness, k = n π/d, n is an odd integer assuming symmetric boundary condition for LSMO, and $k' \approx \pi/d$, and $H_{eff} = 4\pi M_S$ is effective field, The value of H_{eff} =3720 Oe has been used which was extracted from the room temperature FMR data.

The Kittel or uniform excitation mode (k = 0) is always excited in the system and labelled as FMR mode. The perpendicular standing spin wave (PSSW) which is the first mode of above-mentioned Kittel relation (eq. 2) and has already been discussed. The frequency of this mode is very high, and it will thus not intersect the measurement frequency and cannot be detected in our

measurements (see fig 2(b). Further, magnetostatic surface (MSSW) and the backward volume magnetostatic spin waves (BVMSW) excitation requires a highly localized microwave field across the sample which is in contrast to uniform field in our cavity measurements [1].

References

1. V. Flovik, F. Maciá, A. D. Kent, and E. Wahlström, J. Appl. Phys. **117**, 143902 (2015).
2. H. Puszkarski, Prog. Surf. Sci. 9, 191 (1979).
3. C. Kittel, Phys. Rev. **110**, 1295 (1958)
4. X. Liu, Y. Zhou, and J. Furdyna, Phys. Rev. B **75**, 195220 (2007).
5. J. T. Yu, R. A. Turk, and P. E. Wigen, Phys. Rev. B **11**, 420 (1975).
6. C. Kittel Phys. Rev. **73**, 155 (1948).
7. R. Damon and J. Eshbach, Phys. Rev **118**, 1208 (1960).
8. B. A. Kalinikos, IEE Proc. H **127**, 4 (1980).

7.2 Paper II

Mapping the dipolar coupling and magnetodynamic properties of dipole coupled 1D magnonic crystals

S. Singh, X. Wang, A. Kumar, A. Qaiumzadeh, P. Svedlindh, T. Tybell, and E. whalström.

This paper is awaiting publication and is not included in NTNU Open

7.3 Paper III

Pulse versus continuous wave characterization of propagating spin waves in thin magnetic films

S. Singh, V. Furtula, T. Tybell, and E. whalström.

This paper is awaiting publication and is not included in NTNU Open

7.4 Paper IV

Propagation properties of spin wave in Co_2FeAl, half-metallic Heusler alloy, ultrathin film

S. Singh, N. K. Gupta, S. Hait, S. Chaudhary, T. Tybell, and E. whalström.